arXiv:2611.09851v1 [cs.CV] 6 Nov 2026

Health-System-Wide Mapping of Demographic Information in Routine Clinical Histopathology

Shengjia Chen[1,2,†], Ruchika Verma[1,2], Kevin Clare[4], Paula Restrepo[1,2], Jannes Jegminat[1,2], Eugenia Alleva[1,2], Kuan-lin Huang[3], Aryeh Stock[4], Brandon Veremis[4], Thomas Fuchs[1,2], and Gabriele Campanella[1,2,†]

[1]Windreich Department of Artificial Intelligence and Human Health, Icahn School of Medicine at Mount Sinai, New York, USA
[2]Hasso Plattner Institute for Digital Health at Mount Sinai, Icahn School of Medicine at Mount Sinai, New York, USA
[3]Mount Sinai Center for Transformative Disease Modeling, Icahn School of Medicine at Mount Sinai, New York, USA
[4]Department of Pathology, Molecular and Cell-Based Medicine, Mount Sinai Health System, New York, USA
[†]Corresponding author: shengjia.chen@icahn.mssm.edu , gabriele.campanella@mssm.edu

November 9, 2026

Abstract

The extent to which demographic-associated information is detectable across organs and disease states in routine clinical histopathology remains unclear. Here, we analyzed 1.3 million hematoxylin and eosin whole-slide images from 257,322 patients across 25 organs, using pathology foundation-model representations and multiple-instance learning to systematically map information associated with sex, age group, and self-reported race. Across 69 organ–demographic combinations, demographic attributes were broadly recoverable, with pan-organ mean AUROCs of 0.828 for sex, 0.733 for age group, and 0.662 for self-reported race, and substantial variation across organs. Demographic-class balancing produced relatively small changes in performance, while evaluation within diagnosis-text clusters showed modest attenuation. Under training with diagnosis-based grouping, demographic-associated signals remained detectable across multiple organs, including sex in gastric tissue (AUROC 0.865), age group in breast (0.816), and self-reported race in skin (0.728). Literature-guided analysis of these settings generated candidate histomorphological and contextual explanations for further investigation. Together, these findings provide a systematic map of demographic-associated information in routine histopathology, informing investigations of its sources, assessments of potential shortcut learning, and the development of more interpretable computational pathology models.

1 Introduction

Despite more than a century of microscopic examination of human tissue, it remains unknown whether demographic-associated morphologic variation is systematically detectable across organs and disease states. Scattered observations suggest that such variation exists. Sex-associated

nuclear features were described in neurons and neutrophils more than 70 years ago[1,2], and machine-learning models have since estimated chronological age from the histology of healthy tissues and brain[3,4]. More broadly, structural aging mapped from hematoxylin and eosin (H&E) histology of 40 post-mortem tissues in the Genotype-Tissue Expression project followed tissue-specific, nonlinear trajectories, with coordinated deterioration across organs[5]. Race-associated histopathologic and molecular differences have also been reported in organs including skin and prostate[6–8]. These observations establish that demographic-associated variation can have histologic correlates, but the evidence remains fragmented across demographic attributes, organs, and clinical settings. It is therefore unknown how broadly sex, age, and self-reported race are associated with detectable information in routine clinical histopathology across tissues and disease states.

Deep learning provides a means to investigate this question at a scale and sensitivity not readily achievable through conventional morphologic assessment. Computational pathology (CPath) models applied to digitized H&E whole-slide images (WSIs) can identify information associated with disease and tumor grade[9,10], molecular biomarkers and outcomes[11–13], and cellular phenotypes[14,15]. Foundation models (FMs) pretrained on large collections of digitized pathology images[16–20] have further enabled representations that transfer across tasks and centers[21,22]. The ability of these models to recover complex information from routine H&E images raises a fundamental question beyond disease prediction: what information about the patient is encoded in tissue images, including information that may not be apparent to human observers?

Evidence from medical imaging suggests that demographic information can indeed be recovered from images and learned representations[23]. In radiology, self-reported race can be predicted across imaging modalities and external cohorts even when the relevant image features are not apparent to human observers[24]; medical-imaging FMs likewise encode sex, age, and race in their representations[25]. Evidence in histopathology is more limited. Vaidya et al. showed that representations learned for breast and lung cancer subtyping and glioma *IDH1* mutation prediction retained information about patient race[26]. In our prior work in dermatopathology, self-reported race remained predictable under the evaluated disease-distribution controls, with attention and ablation analyses implicating the epidermis as one source of predictive signal[27]; pigmentation-related epidermal features are one plausible candidate correlate[6]. Together, these findings indicate that demographic information can be present in medical images and learned representations, but they do not establish how broadly such information is detectable across routine histopathology or which histologic features carry it.

Establishing the extent of demographic predictability also has important implications for the development and evaluation of CPath models. If demographic attributes are recoverable from H&E images or their learned representations, this information is potentially available to models even when demographic variables are not explicitly provided as inputs. Models may then exploit demographic-associated information when it correlates with a prediction target, creating the possibility of shortcut learning[28,29]. Performance disparities have been documented in medical imaging and CPath[25,26,30]; a pan-cancer analysis, for example, reported significant disparities across self-reported race, gender, or age groups in 29.3% of diagnostic tasks[31]. Self-reported race may serve as an imperfect proxy for genetic ancestry, while also capturing social, environmental, and healthcare-related factors. Demographic predictability does not by itself demonstrate that a clinical model uses demographic information, just as an observed performance disparity does not establish demographic proxy use. Rather, determining where demographic information is recoverable identifies settings in which such use is possible and can be tested directly.

A central challenge is that demographic predictability need not arise from intrinsic tissue morphology. Demographic groups can differ in disease prevalence, specimen and case mix, healthcare context, and other cohort characteristics, while tissue processing, staining, scanning, and image acquisition can introduce additional correlations[28,29,32]. The Cancer Genome Atlas illustrates this

problem: contributing sites differ in clinical and demographic composition, while their digital slides carry site-specific visual signatures arising from both biological differences and non-biological batch effects[26,32,33]. Deep learning models can recover the submitting site from digitized slide images, and these signatures remain detectable after commonly used stain normalization and augmentation[32,34]. When the same cohort structure is represented in training and validation data, such associations can remain hidden and produce optimistic estimates of performance that deteriorate when site, case mix, or acquisition conditions change[28,29,32,35]. Consequently, mapping demographic-associated image information requires testing whether predictability persists when major sources of cohort structure, particularly demographic-class imbalance and diagnosis context, are constrained. Even when it persists, predictability alone does not identify its causal source; residual signals may reflect tissue-associated features, clinical or sampling context, acquisition effects, or combinations of these factors.

Here, we address a fundamental question: to what extent are basic demographic attributes encoded in tissue morphology across the human body? To that end, we analyzed 1,302,440 H&E WSIs from 257,322 patients across 25 organs in the Mount Sinai Health System to systematically map demographic-associated information in routine clinical histopathology. Using pathology FM features and attention-based multiple-instance learning (MIL), we evaluated sex, age group, and self-reported race across 69 organ–demographic combinations. Complementary controls assessed demographic-class exposure balancing, diagnosis-constrained versus non-stratified grouped training, and within-diagnosis evaluation. These comparisons characterize the sensitivity of demographic predictability to the evaluated controls without partitioning the signal into causal components. Selected residual signals were further examined through targeted literature searching to generate testable hypotheses for subsequent morphologic investigation. This study maps where demographic information is image-predictable, where it persists under diagnosis and cohort controls, and which residual signals warrant further morphologic investigation. It thereby provides a systematic foundation for studying demographic-associated variation in human histopathology and its implications for downstream CPath models.

2 Methods

Study design and cohort

This retrospective cohort included all available digitized routine diagnostic H&E WSIs from the Mount Sinai Health System (MSHS) through October 2025, together with linked pathology reports and clinical metadata. Cases without digitized H&E WSIs were excluded. The finalized cohort comprised 257,322 patients, 327,483 pathology cases, 731,972 specimens, and 1,302,440 WSIs. The data followed a hierarchical structure: each patient could contribute one or more cases, each case with one or more specimens, and each specimen with one or more WSIs. De-identified identifiers preserved these links. Routine staining and scanning were centralized within MSHS. This study was approved by the Institutional Review Board at the Icahn School of Medicine at Mount Sinai (Protocol STUDY-20-00338). Informed consent was waived under the approved protocol.

Report extraction and organ grouping

Model development and evaluation were stratified by specimen organ. Pathology reports were linked to cases and parsed at the specimen level using OpenAI GPT-5 mini[36], accessed through Azure OpenAI. Schema-constrained outputs recorded each specimen's anatomic source, normalized

organ label, and verbatim diagnosis text. The extraction protocol is summarized in Supplementary Note S1.

Extracted organ labels were normalized into 25 groups selected for clinical interpretability and sufficient data for model training and evaluation. Closely related anatomic sites were consolidated where appropriate, including colon/rectum, bone/joint, and soft tissue. Specimens not mapped to these groups were assigned to an Other category and excluded from pan-organ analyses. The final organ set included bladder, bone marrow, bone/joint, brain, breast, cervix, colon/rectum, esophagus, gallbladder, gastric, kidney, liver, lung, lymph node, mouth, ovary, pancreas, placenta, prostate, sinus, skin, small bowel, soft tissue, thyroid, and uterus. For the cohort overview, specimen-level diagnosis text was visualized using UMAP and classified into four broad categories (neoplastic, normal, inflammatory, and other) using rule-based text mapping (Fig. 1B). Details are provided in Supplementary Note S2.

Demographic labels

Eligibility was determined separately for each demographic target based on the availability of a valid label. Sex was recorded at the patient level and harmonized to female and male; indeterminate or unknown labels were excluded. Sex prediction was evaluated across 19 organ groups, excluding prostate, breast, cervix, ovary, uterus, and placenta. Self-reported race was recorded at the patient level and harmonized to five mutually exclusive categories: White, Black or African American, Hispanic or Latino, Asian, and Other. Other included Native Hawaiian or Other Pacific Islander, American Indian or Alaska Native, and Other Race; missing or unmappable values were excluded. Age at the pathology encounter was calculated as case receive year minus birth year and grouped into 20–34, 35–44, 45–54, 55–64, 65–74, and $\geq$75 years. Cases with missing age or age below 20 years were excluded from age-group analyses.

Diagnosis embeddings and clustering

Diagnosis text embeddings were used to group specimens with similar diagnostic contexts for stratified evaluation of demographic predictability and the construction of cluster-constrained training groups. Specimen-level diagnosis text was encoded using OpenAI `text-embedding-3-large`, producing 3,072-dimensional embeddings. Embeddings were computed at the specimen level because a single pathology case may contain multiple specimens from different anatomic sites with distinct diagnoses. For each organ, we applied k-means clustering to the diagnosis embeddings. The number of clusters was selected separately from an organ-specific candidate grid using silhouette scores. K-means was fit once per organ, over all eligible specimens for that organ. The resulting assignments were fixed across all Monte Carlo cross-validation (MCCV) folds.

Controlled training regimes

The overall study design is summarized in Fig. 2A. Observed-distribution training (S1) sampled cases according to the observed demographic-class distribution. Demographic-balanced training (S2) used case-level resampling to balance demographic-class exposure, using the S1 epoch-size target. Diagnosis-context-constrained grouped training (S3) constructed demographic-balanced groups within diagnosis clusters in each fold's training pool. Retained classes were oversampled to the largest class before assembling groups containing one case from each retained class.

For group construction, specimen-level cluster assignments were mapped to cases by majority vote, with ties resolved by the first tied cluster encountered in specimen row order. The random grouped-training control ($S3_{RND}$) applied the same demographic balancing procedure to the full

training pool without diagnosis-context constraints. This comparison assessed the additional association of diagnosis-context constraints under grouped training; it did not isolate data size or guarantee identical training exposure. Detailed group-construction, class-retention, and epoch-exposure rules are provided in Supplementary Method 1.1. All regimes shared the same model architecture, prediction unit, and cross-validation design.

Model development

For each case and organ target, eligible H&E slides from organ-matched specimens were combined into one case-level MIL bag, capped at 30 slides and 100,000 tiles. For cases exceeding the 30-slide cap, slides were randomly subsampled at each training epoch using a seeded random procedure. At least one organ-matched specimen with linked H&E WSIs was required for inclusion. GrandQC[37] excluded background, pen marks, and artifacts before tile extraction at 20× magnification. The in-house small vision transformer (ViT-small) pathology foundation model SP22M[38] generated 384-dimensional tile embeddings without task-specific fine-tuning.

Gated multi-head attention MIL used class-specific attention heads[39,40]. Models were trained with AdamW, a learning rate of 10^{-5}, 10 epochs of linear warm-up, and cosine decay to 10^{-6} over 50 epochs. S1 and S2 processed one case at a time and computed case-level losses, whereas S3 and its random grouped-training control summed case-level losses across group members before gradient accumulation and optimizer updates. Detailed regime-specific loss aggregation, epoch-exposure formulas, and group caps are provided in Supplementary Method 1.1.

Evaluation and statistical analysis

Performance was estimated using 10-fold MCCV, with an 80/20 train-validation split per fold. Sex and self-reported race used patient-level splits, whereas age group used case-level splits to account for age variation across encounters. Evaluation was performed at the case level. All models were evaluated at the final training epoch (epoch 50).

The primary metric was macro one-vs-rest area under the receiver operating characteristic curve (AUROC), reported as mean ± standard deviation (SD) across folds. Regime comparisons emphasized paired AUROC differences and their consistency across organs and folds. Paired t-tests were performed across matched MCCV folds, with Benjamini–Hochberg (BH) adjustment applied separately within each demographic target and regime comparison. Statistical results are provided in Supplementary Table S10.

As an additional evaluation analysis, the existing S1 and S2 predictions were evaluated within diagnosis-text clusters using the same matched validation cases as pooled evaluation. Within-cluster AUROCs were aggregated using case-count weighting and compared with pooled AUROC. This analysis introduced neither a new training regime nor a prediction target and was distinct from diagnosis-context-constrained S3 training. Clusters containing fewer than two target classes were excluded. The same evaluation procedure was applied across all organ and demographic combinations, including the breast case study. Detailed definitions and eligibility criteria are provided in Supplementary Method 1.2.

Literature searching and hypothesis generation

Targeted large language model (LLM)-assisted literature searching was conducted for the three selected organ–demographic combinations to identify potential histomorphologic and clinical explanations for residual demographic predictability. Using OpenAI `gpt-6-astra` (accessed 24 September

2026), a standardized prompt was used to identify relevant studies, including supporting, contradictory, and null findings. Candidate explanations were checked in a separate model-assisted pass against retrieved abstracts or accessible full texts for citation accuracy, evidence support, and applicability to the study population and tissue context. The resulting literature-supported hypotheses were summarized to guide subsequent morphologic investigation. The search protocol and source verification procedures are provided in Supplementary Method 1.3.

3 Results

Cohort characteristics

The study cohort comprised 257,322 patients, 327,483 surgical and biopsy cases, 731,972 pathology specimens, and 1,302,440 digitized H&E WSIs from MSHS in New York City (NYC) through October 2025 (Fig. 1). Among patients with known sex (n = 255,382), 159,411 (62.4%) were female and 95,971 (37.6%) male. Among patients with known self-reported race/ethnicity (n = 207,500), 90,761 (43.7%) were White, 47,220 (22.8%) Hispanic or Latino, 36,388 (17.5%) Black or African American, 18,457 (8.9%) Asian, and 14,674 (7.1%) Other. In the 2024 NYC ACS population (n = 8,478,072), provided as an external demographic reference and not included in the study cohort, 30.7% were non-Hispanic White, 28.7% Hispanic or Latino, 20.0% non-Hispanic Black or African American, and 15.1% non-Hispanic Asian[41]. Among cases with known age (n = 318,174), 48,126 (15.1%) were aged 20–34 years, 50,160 (15.8%) 35–44, 58,635 (18.4%) 45–54, 64,503 (20.3%) 55–64, 59,356 (18.7%) 65–74, and 37,394 (11.8%) ≥75 (Fig. 1A). Full distributions and missing-label categories are reported in Supplementary Table S1.

The diagnostic spectrum included neoplastic, normal, inflammatory, and other findings across the study organs. Among the 679,940 mapped specimens, 26.0% were neoplastic, 24.5% normal, 21.2% inflammatory, and 28.4% other, including indeterminate findings (Fig. 1B; Supplementary Note S2). Specimens spanned 25 organ groups organized into 13 pathology subspecialty divisions. The largest groups were colon/rectum (144,880 specimens), breast (75,781), gastric (67,104), and prostate (58,135) (Fig. 1C; Supplementary Table S2). Per-organ demographic composition is reported in Supplementary Table S3.

Pan-organ demographic predictability

Demographic predictability under observed-distribution training (S1) was widespread but varied across organs and targets. Across 69 organ–demographic combinations (25 age-group, 25 self-reported-race, and 19 sex tasks), each evaluated over ten MCCV splits, sex had the highest pan-organ mean AUROC ± inter-organ SD: 0.828 ± 0.119 (range, 0.594–0.970). Age group followed at 0.733 ± 0.084 (range, 0.545–0.882), then self-reported race at 0.662 ± 0.074 (range, 0.526–0.793; Fig. 2B; Supplementary Table S4). The interactive Pan-organ Results Atlas provides a companion visualization of aggregate organ- and demographic-specific results across training controls.

Organ-level performance differed within as well as across the subspecialty groups in Fig. 1C. Across the four gastrointestinal organs, sex AUROC was highest in gastric tissue (0.970) and colon/rectum (0.965), followed by small bowel (0.942) and esophagus (0.872). Breast had the highest age-group AUROC (0.882); all three gynecologic organs also had high age-group performance (ovary and uterus, 0.850; cervix, 0.834), but lower self-reported-race performance (0.588–0.653). Self-reported-race AUROC was highest in skin (0.793), with gastric tissue and colon/rectum also among the highest-performing organs (0.776 and 0.759). Pancreas had the lowest AUROC for all

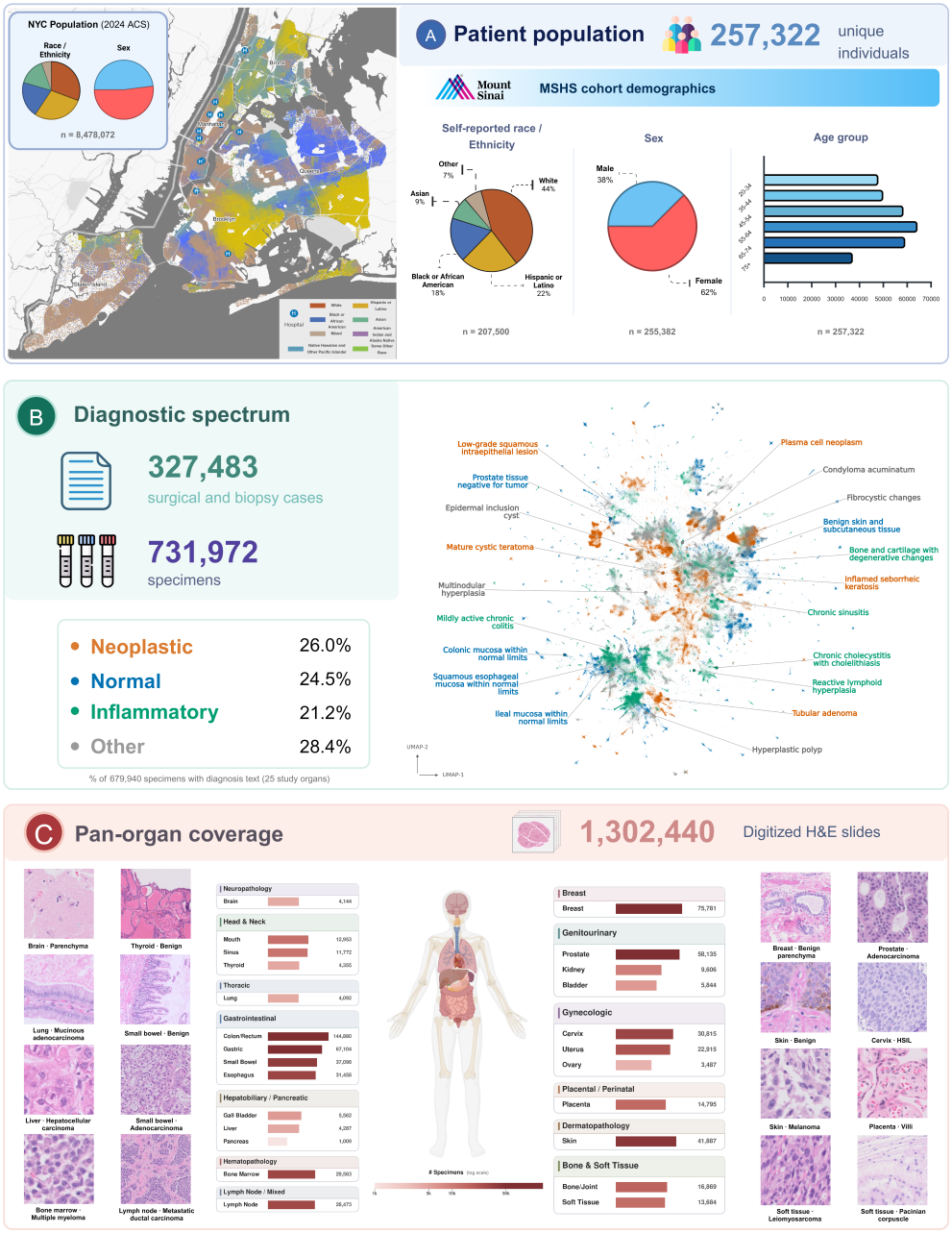


Figure 1: **Scale and diversity of the MSHS routine histopathology cohort. (A) Population context.** NYC geography and cohort demographics. ACS percentages use all residents: Hispanic/Latino of any race and non-Hispanic White, Black, and Asian; remaining categories differ from cohort Other. Cohort age is case-level. **(B) Diagnostic spectrum.** Diagnosis-text UMAP and percentages for 679,940 specimens from 25 organs. Colours: neoplastic, orange; normal, blue; inflammatory, green; other (including indeterminate), grey. Labels identify diagnoses; dense islands reflect templated sign-out text, not prevalence. **(C) Pan-organ coverage.** The cohort comprises 1,302,440 digitized H&E slides. Bars show specimen counts across 25 organs grouped into 13 pathology subspecialty divisions, on a shared logarithmic scale (color saturation at $\geq$50,000 specimens). Sixteen illustrative H&E images highlight histological diversity across organs. Created in BioRender. Chen, S. (2026) https://BioRender.com/pc3001s

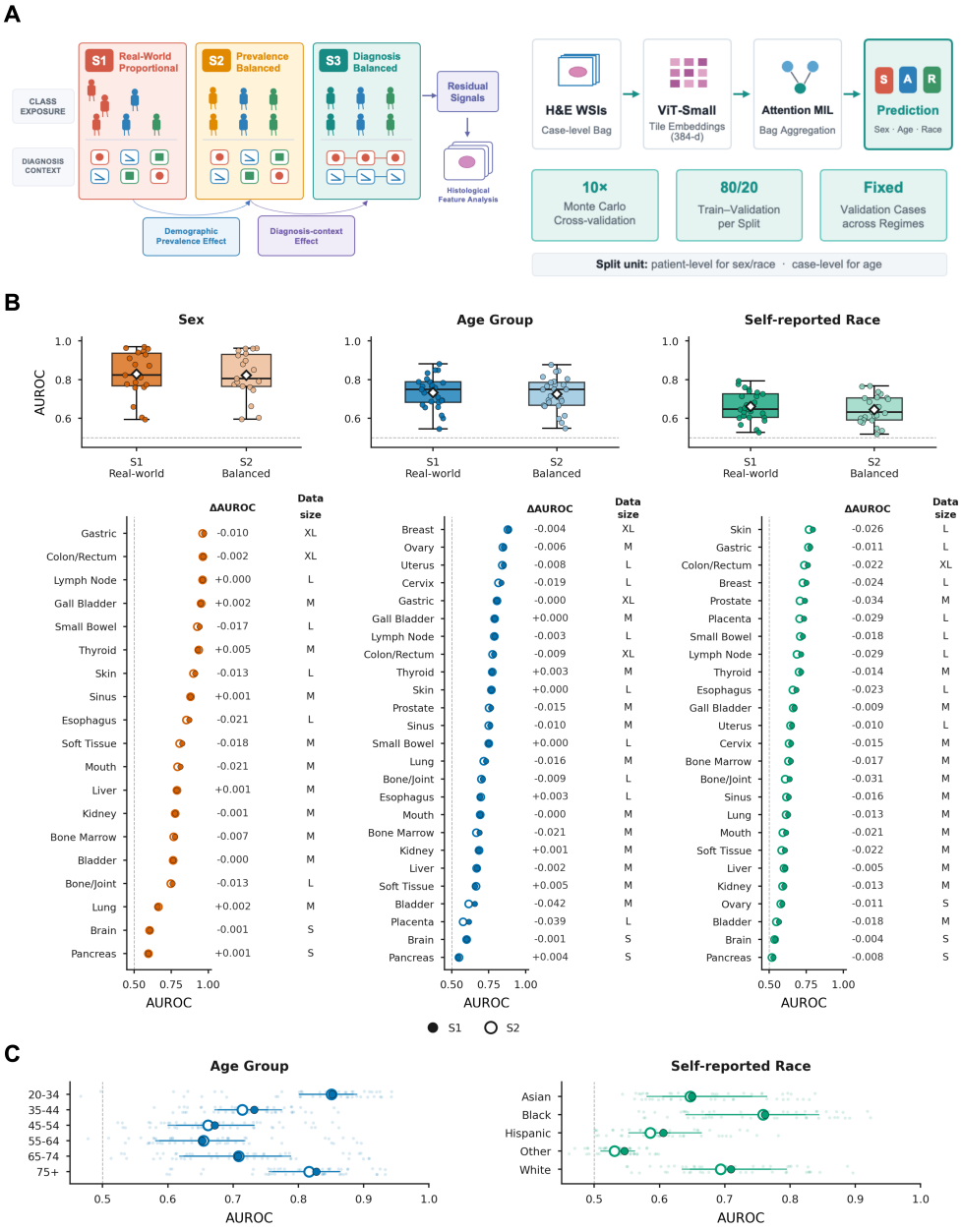


Figure 2: **Experimental framework and pan-organ demographic signal across organs. (A) Experimental framework.** S1 (observed-distribution), S2 (demographic-balanced), and S3 (diagnosis-context grouped) case-level prediction: organ-matched H&E slides, quality control, 20× tiling, in-house ViT-Small (SP22M) features, and gated multi-head AB-MIL. **(B) Pan-organ performance.** S1/S2 AUROC distributions (top) and paired organ comparisons (bottom), with mean ΔAUROC (S2−S1) across 10 matched MCCV folds and size tiers. Tiers use mean S1 training-case counts across folds per organ and target: XS, < 500; S, 500–$< 2{,}000$; M, 2,000–$< 10{,}000$; L, 10,000–$< 30{,}000$; XL, $\geq 30{,}000$. **(C) Subgroup performance.** Age-group and self-reported-race AUROC under S1/S2. Large markers and horizontal bars denote cross-organ medians and interquartile ranges; background points show individual organs.

three targets: 0.594 for sex, 0.545 for age group, and 0.526 for self-reported race (Supplementary Table S4).

Demographic predictability under class balancing

Compared with S1, demographic-balanced training (S2) produced small reductions in pan-organ mean AUROC: 0.006 for sex (0.822 versus 0.828), 0.007 for age group (0.726 versus 0.733), and 0.018 for self-reported race (0.644 versus 0.662; Fig. 2B; Supplementary Table S4). The reduction was most consistent for self-reported race: all 25 organs showed lower AUROC (median difference, −0.017; range, −0.034 to −0.004), and 16 were lower in all ten matched folds (Fig. 2B). Age and sex showed smaller, more heterogeneous changes, with median differences of −0.003 and −0.001 and lower AUROC in 17 of 25 and 12 of 19 organs, respectively. Exploratory paired tests and BH-adjusted results are reported in Supplementary Table S10.

Age-group AUROC followed an approximately U-shaped pattern under both S1 and S2, with higher performance in the youngest and oldest groups. Self-reported-race performance was heterogeneous, with Black or African American and White generally higher and Other near chance; S2 largely preserved this subgroup ordering despite modest overall attenuation. Performance did not simply track training-set abundance: the largest age groups had lower AUROC than the less frequent age extremes, and White had more training cases but lower AUROC than Black or African American (Fig. 2C; Supplementary Table S5).

Diagnosis context and within-cluster predictability

Because diagnosis composition may contribute to demographic predictability, we examined whether demographic-associated information remained detectable when evaluation was restricted to cases with similar diagnostic contexts. Breast served as a worked example for examining demographic composition and predictability within diagnosis contexts. Diagnosis-text embeddings were grouped into ten clusters linked to 46,145 unique cases (Fig. 3A–C). Diagnosis-text patterns included fibrocystic changes with calcifications, invasive carcinoma, fibroadenoma, and benign parenchyma. Demographic composition varied across clusters. Ages 20–34 accounted for 30.3% of cases with known age in the fibroadenoma cluster, compared with 10.2% across the breast cohort, an enrichment of 20.1 percentage points. In the invasive-carcinoma cluster, ages ≥ 75 accounted for 23.6% versus 12.5% overall (Fig. 3C). Associations between diagnosis-cluster membership and demographic composition were also observed across organs (Supplementary Table S6); cluster-level demographic frequencies can also be explored in the interactive Pan-organ Results Atlas.

Within-cluster evaluation produced modest attenuation of breast demographic predictability. AUROC was computed within diagnosis clusters and aggregated using case-count weighting for comparison with pooled validation AUROC. Under S1, age-group AUROC decreased from 0.882 pooled to 0.874 cluster-stratified, and self-reported-race AUROC from 0.750 to 0.743, with attenuation of 0.007–0.008 under both S1 and S2 (Fig. 3D). Associations between subgroup enrichment and within-cluster AUROC were negative for all six age groups and mixed in sign for self-reported race (Fig. 3E).

Across all 69 organ–demographic combinations, within-cluster evaluation using the primary silhouette-selected K produced mean AUROC reductions of 0.0216 for age group, 0.0121 for self-reported race, and 0.0095 for sex under S1, and 0.0190, 0.0118, and 0.0098, respectively, under S2. The evaluation-only random-label control remained within 0.001 of zero in aggregate (Supplementary Tables S7–S8; Supplementary Fig. S2).

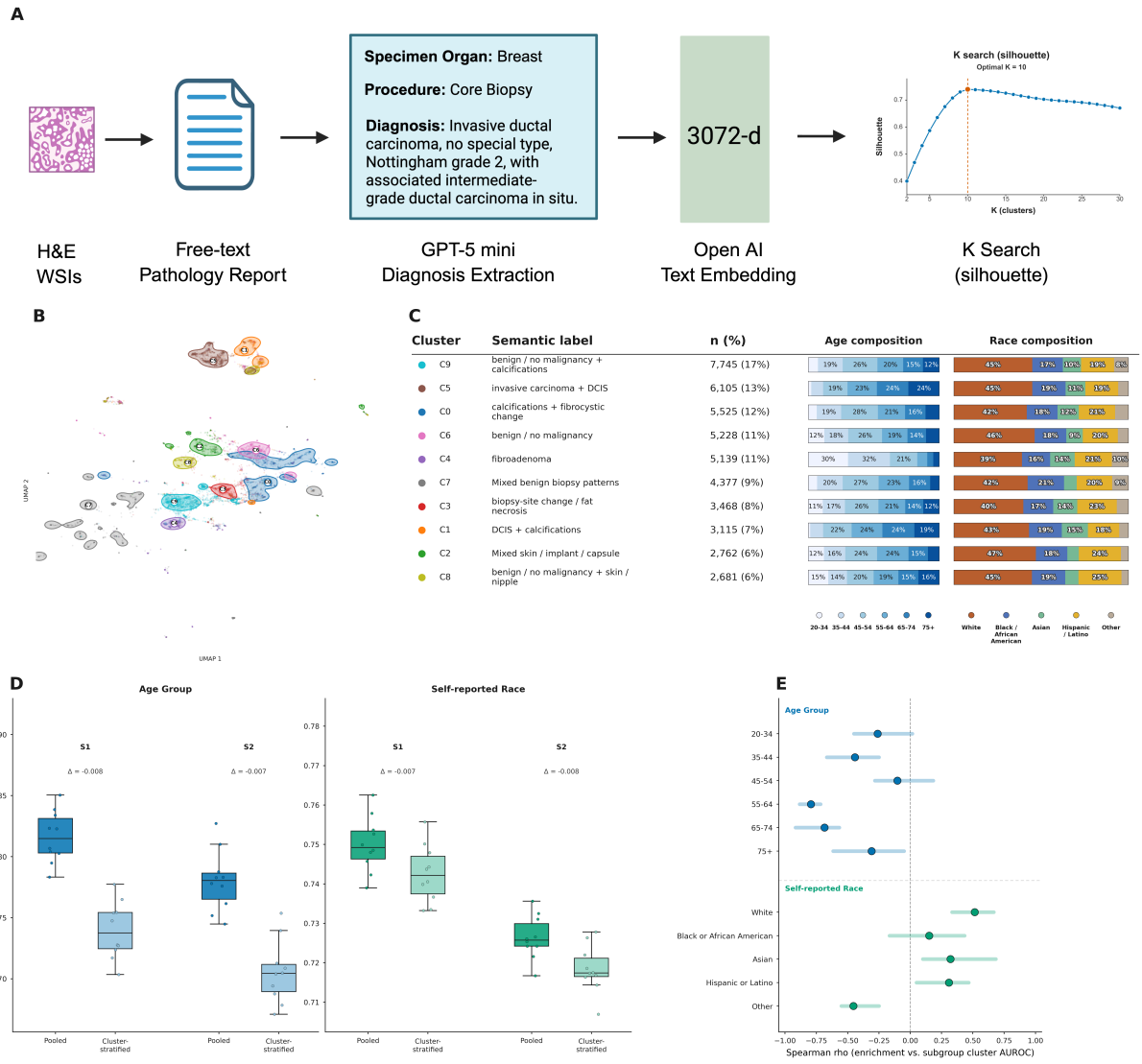


Figure 3: **Breast as a worked example of diagnosis-context stratification. (A) Diagnosis-context pipeline.** Free-text pathology reports were parsed into specimen-level diagnoses, encoded as 3,072-dimensional text embeddings, and grouped by k-means clustering; the number of clusters was selected by silhouette analysis. **(B) Diagnosis-cluster map.** Uniform manifold approximation and projection (UMAP) of the resulting $K = 10$ breast diagnosis clusters, shown by kernel-density contours. **(C) Cluster composition.** Cluster size, semantic label, and age-group and self-reported-race composition across 46,145 unique breast cases, ranked by cluster size; age and race proportions use 45,750 and 29,343 known-label cases, respectively. Labels summarize diagnosis-text patterns and were not independently validated by pathologists. Panels B–E use canonical $K = 10$ assignments. **(D) Cluster-stratified performance.** Pooled validation AUROC versus case-count-weighted within-cluster (cluster-stratified) AUROC for age group and self-reported race under S1 and S2. Boxes summarize 10 MCCV folds; annotations show the stratified-minus-pooled difference (Δ). **(E) Enrichment–performance association.** Spearman correlation between subgroup enrichment (percentage points relative to the eligible breast cohort) and within-cluster subgroup AUROC under S1; horizontal bars show leave-one-cluster-out sensitivity ranges.

Predictability under diagnosis-context grouped training

Cluster-constrained grouped training (S3) yielded modestly lower pan-organ AUROC than grouped demographic balancing without diagnosis constraints ($S3_{RND}$). We define the signed AUROC difference as $\Delta AUROC = AUROC(S3_{RND}) - AUROC(S3)$, so positive values indicate lower performance under cluster-constrained training. Mean differences were +0.005 for sex, +0.017 for age group, and +0.013 for self-reported race (Fig. 4A; Supplementary Table S9). Residual S3 pan-organ mean AUROCs were 0.697, 0.653, and 0.594, respectively, using the matched S3 evaluation population for age (Fig. 4; original regime-specific values are retained in Supplementary Table S4). The prostate age comparison used four common classes and matched validation cases, with an AUROC difference of 0.014 (Supplementary Method 1.4.1).

Relative to S2, $S3_{RND}$ had lower mean AUROC for sex (0.702 versus 0.822, a difference of −0.121) and self-reported race (0.607 versus 0.644, a difference of −0.037); the corresponding S3 differences were −0.126 and −0.050. These comparisons reflect broader training-regime differences. Pan-organ S2/S3 age comparisons were omitted because evaluation class sets differed in prostate and placenta (Supplementary Method 1.4.1).

Residual predictability and its sensitivity to diagnosis constraints varied across the 69 combinations with comparable S3 evaluations (Fig. 4B). Sex prediction in gastric tissue retained an AUROC of 0.865 with little difference between regimes (−0.003), whereas sex prediction in lymph nodes retained 0.827 with a larger difference (+0.027). Age-group prediction in breast and prediction of self-reported race in skin retained AUROCs of 0.816 and 0.728, with differences of +0.002 and +0.030, respectively.

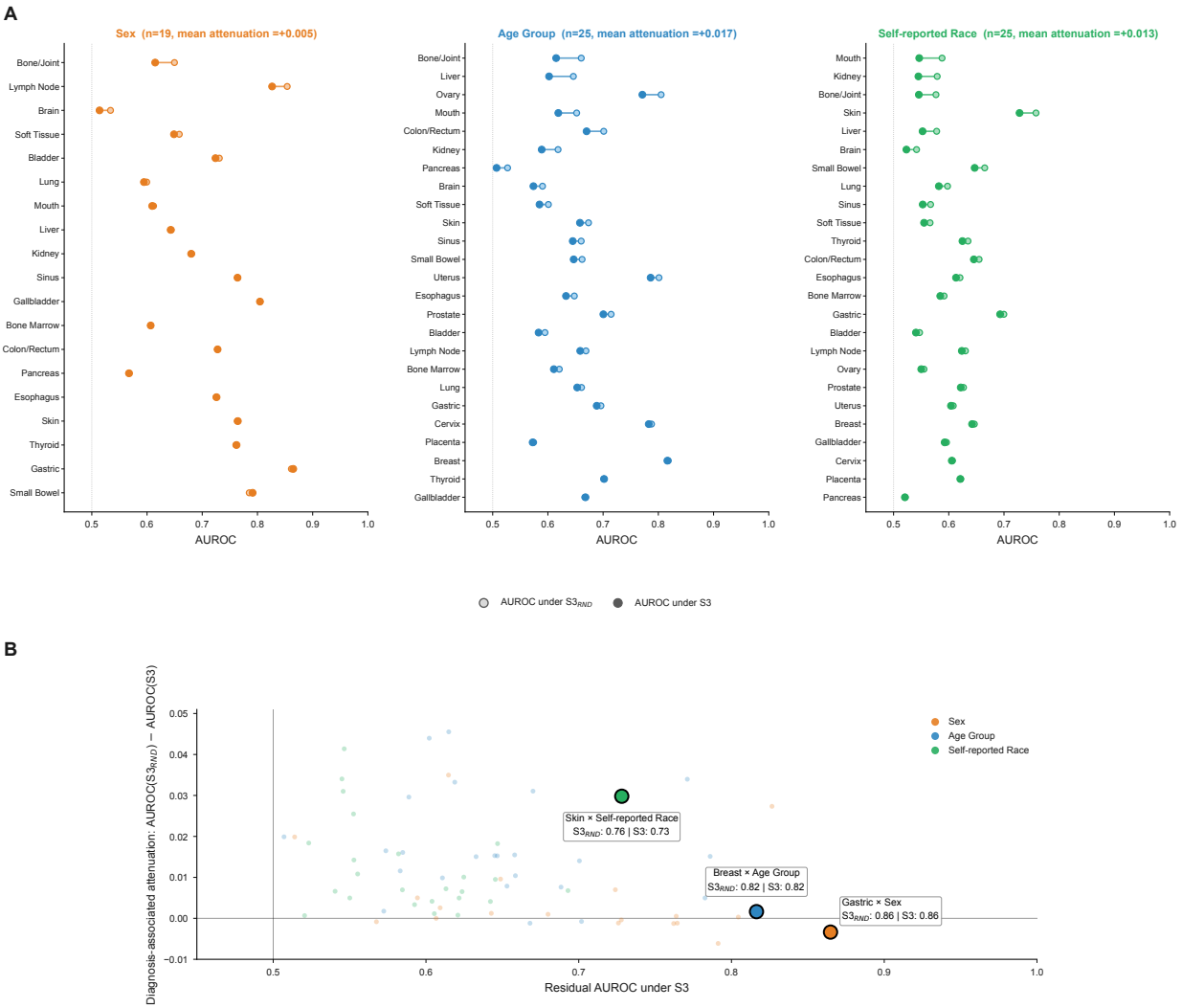


Figure 4: **Residual demographic predictability under diagnosis-context grouped training.** **(A)** Paired organ-level $S3_{RND}$ and S3 AUROC, ranked by the signed AUROC difference (19 sex, 25 age-group, and 25 self-reported-race tasks). Prostate age uses four common classes and 1,954 matched validation cases per fold; placenta age uses three classes and 2,872 matched cases. All S3 comparisons use epoch-50 evaluation (Supplementary Method 1.4.1). Markers distinguish the two training regimes; exploratory paired tests and BH-adjusted results are reported in Supplementary Table S10. **(B)** Residual S3 AUROC versus the difference, $\text{AUROC}(S3_{RND}) - \text{AUROC}(S3)$, across 69 combinations; positive values indicate lower S3 AUROC. Prostate age uses the harmonized S3 AUROC and difference; all other points retain their original evaluation definitions.

Literature-guided hypotheses for selected signals

We developed the public SAIF Hypothesis Explorer to organize candidate explanations and supporting, contradictory, and limiting literature, and to facilitate further investigation and community discussion. Candidates were generated through targeted LLM-assisted literature searching followed by source checking (Literature searching and hypothesis generation). Sex prediction in gastric tissue, age-group prediction in breast, and prediction of self-reported race in skin received detailed attention because of their substantial residual performance and value as representative settings for further histomorphological investigation.

For sex prediction in gastric tissue, selected gastric cancer cohorts support sex differences in subtype composition[42,43], while studies of *Helicobacter pylori*-associated and benign gastric disease suggest context-dependent mucosal differences related to infection, subsite, and eradication history[44,45]. These findings identify cancer subtype composition and mucosal disease context as candidate explanations for the retained signal.

For age-group prediction in breast, retained performance motivated review of age-associated tissue changes. Terminal duct lobular unit (TDLU) involution[46,47] and H&E morphometry[48] support differences in epithelial cellularity and stromal/adipose composition as candidate correlates. Reported associations between parity and lobular measures indicate that such features are not specific to chronological age[49]. These observations are cross-sectional and do not establish that the model uses these features.

For prediction of self-reported race in skin, substantial retained predictability motivated investigation of both tissue and sampling context. Epidermal pigmentation emerged as a candidate tissue correlate, supported by studies of epidermal melanin and melanosome distribution[50,51]. Some supporting evidence used modalities or population definitions that do not map directly to routine H&E or the categories used here; anatomical-site and exposure differences remain contextual alternatives, and measured ultraviolet sensitivity has been reported to predict photodamage better than racial or ethnic origin[52]. Differential biopsy practice is a further contextual candidate: within psoriasis, biopsy frequency has been reported to differ by race and ethnicity[53], and selected psoriasis biopsy series document a broad histological spectrum[54], so diagnosis- and indication-specific sampling could alter the lesion mix across label groups.

4 Discussion

This study systematically mapped demographic-associated information recoverable from routine clinical histopathology across 25 organs and 69 organ–demographic combinations. Using deep learning models as analytical tools, we found that information associated with sex, age group, and self-reported race was broadly detectable, although its recoverability varied substantially across organs and demographic attributes. Demographic-class balancing produced relatively small changes in model performance, and additional diagnosis-context analyses showed modest attenuation while leaving substantial signals in multiple tissues. Together, these findings establish a pan-organ reference for investigating demographic-associated variation in histopathology and its implications for computational pathology research.

Demographic-associated information in clinical histopathology may reflect differences in demographic representation and diagnostic composition, in addition to tissue-associated characteristics. To examine the sensitivity of the observed signals to these factors, we compared observed-distribution training (S1) with demographic-balanced training (S2), which produced relatively small changes in performance. Evaluation within diagnosis-text clusters further showed modest attenuation relative to pooled evaluation. Under grouped training, introducing diagnosis-context constraints (S3) yielded

additional, generally modest attenuation compared with random grouping without these constraints ($S3_{RND}$). Notably, substantial demographic-associated signals remained across multiple organs under the evaluated controls, motivating further investigation of tissue-associated information and clinical or contextual factors not captured by these analyses.

The heterogeneity of demographic-associated information across organs raises questions about the histological and contextual features underlying these signals. Such information may be localized to specific tissue compartments, reflected in cellular morphology, or distributed across broader tissue regions. To facilitate further investigation, we selected three representative settings—sex in gastric tissue, age group in breast, and self-reported race in skin—and used literature-guided searching to identify plausible histomorphological and clinical correlates. Our previous dermatopathology study, in which attention and ablation analyses highlighted the epidermis as an important region for self-reported-race classification, illustrates how spatial analyses can help investigate candidate sources of information[27]. The hypotheses assembled here provide starting points for targeted pathology review, quantitative feature measurement, and diagnosis-matched analyses, while inviting further investigation of alternative explanations and previously unrecognized tissue-associated patterns.

The widespread availability of demographic-associated information in histopathology has implications for computational pathology model development and clinical translation. Such information may provide useful context for certain clinical tasks, but it may also become a source of shortcut learning when models exploit demographic correlations that do not generalize across populations or care settings[28,29]. Whether these associations are informative or problematic depends on the intended task, the model's use of the information, and the population in which it is applied. Our findings therefore support more systematic characterization of patient populations and demographic subgroup performance during model development and evaluation[26,31]. Where data permit, studies should report performance across relevant demographic groups, including self-reported race, sex, and age. At a minimum, clear reporting of cohort demographic composition and population restrictions can help researchers assess the applicability of a model to new clinical settings. The pan-organ map presented here may help prioritize organ-specific investigations, subgroup validation, and assessments of potential demographic shortcuts in downstream pathology models.

Several considerations remain important for interpreting these findings. Self-reported race may serve as an imperfect proxy for genetic ancestry while also reflecting social, environmental, and healthcare-related factors. Future studies incorporating ancestry-informed measures could provide complementary perspectives on the sources of demographic-associated information in histopathology. The single-health-system cohort provided a relatively consistent clinical and imaging environment, although independent cohorts will be important for evaluating the reproducibility of organ-specific patterns. Diagnosis-text clustering captured broad diagnostic contexts but could not fully account for disease heterogeneity, clinical history, sampling practices, or other potential confounders. The present study also did not directly localize the histological features underlying the observed signals. Future investigations combining more granular clinical stratification with tissue-region, tile-level, and cellular analyses may help identify the morphological and contextual sources of demographic-associated information. By providing a systematic map and literature-informed candidate hypotheses, this study offers a foundation for further investigation of these signals and their relevance to computational pathology.

Ethics approval

This retrospective study was approved by the Institutional Review Board at the Icahn School of Medicine at Mount Sinai (Protocol STUDY-20-00338). Informed consent was waived under the

approved protocol.

Data availability

Two complementary interactive resources accompany the manuscript: the Pan-organ Results Atlas for aggregate organ- and demographic-specific results, and the SAIF Hypothesis Explorer for candidate explanations, supporting and limiting literature, and community discussion. The hypotheses are proposed explanations, not validated findings.

References

[1] Barr, M. L. & Bertram, E. G. A morphological distinction between neurones of the male and female, and the behaviour of the nucleolar satellite during accelerated nucleoprotein synthesis. *Nature* **163**, 676–677 (1949).

[2] Davidson, W. M. & Smith, D. R. A morphological sex difference in the polymorphonuclear neutrophil leucocytes. *BMJ* **2**, 6–7 (1954).

[3] Meng, R. *et al.* Machine-learning models based on histological images from healthy donors identify imageQTLs and predict chronological age. *Proc. Natl Acad. Sci. USA* **122**, e2423469122 (2025).

[4] Marx, G. A. *et al.* Histopathologic brain age estimation via multiple instance learning. *Acta Neuropathol.* **146**, 785–802 (2023).

[5] Yadav, A., Alvarez, K., Chechenina, A. *et al.* Mapping structural aging across human tissues reveals tissue-specific trajectories and coordinated deterioration. *Nat. Aging* **6**, 2013–2027 (2026).

[6] Williams, K. A., Wondimu, B., Ajayi, A. M. & Sokumbi, O. Skin of color in dermatopathology: does color matter? *Hum. Pathol.* **140**, 240–266 (2023).

[7] Bigler, S. A., Pound, C. R. & Zhou, X. A retrospective study on pathologic features and racial disparities in prostate cancer. *Prostate Cancer* **2011**, 1–7 (2011).

[8] Awasthi, S. *et al.* Comparative genomics reveals distinct immune-oncologic pathways in African American men with prostate cancer. *Clin. Cancer Res.* **27**, 320–329 (2021).

[9] Campanella, G. *et al.* Clinical-grade computational pathology using weakly supervised deep learning on whole slide images. *Nat. Med.* **25**, 1301–1309 (2019).

[10] Bulten, W. *et al.* Artificial intelligence for diagnosis and Gleason grading of prostate cancer: the PANDA challenge. *Nat. Med.* **28**, 154–163 (2022).

[11] Kather, J. N. *et al.* Deep learning can predict microsatellite instability directly from histology in gastrointestinal cancer. *Nat. Med.* **25**, 1054–1056 (2019).

[12] Campanella, G. *et al.* Real-world deployment of a fine-tuned pathology foundation model for lung cancer biomarker detection. *Nat. Med.* **31**, 3002–3010 (2025).

[13] Volinsky-Fremond, S. *et al.* Prediction of recurrence risk in endometrial cancer with multimodal deep learning. *Nat. Med.* **30**, 1962–1973 (2024).

[14] Graham, S. *et al.* Hover-Net: Simultaneous segmentation and classification of nuclei in multi-tissue histology images. *Med. Image Anal.* **58**, 101563 (2019).

[15] Hörst, F. *et al.* CellViT: Vision transformers for precise cell segmentation and classification. *Med. Image Anal.* **94**, 103143 (2024).

[16] Chen, R. J. *et al.* Towards a general-purpose foundation model for computational pathology. *Nat. Med.* **30**, 850–862 (2024).

[17] Xu, H. *et al.* A whole-slide foundation model for digital pathology from real-world data. *Nature* **630**, 181–188 (2024).

[18] Vorontsov, E. *et al.* A foundation model for clinical-grade computational pathology and rare cancers detection. *Nat. Med.* **30**, 2924–2935 (2024).

[19] Ding, T. *et al.* A multimodal whole-slide foundation model for pathology. *Nat. Med.* **31**, 3749–3761 (2025).

[20] Lu, M. Y. *et al.* A visual-language foundation model for computational pathology. *Nat. Med.* **30**, 863–874 (2024).

[21] Campanella, G. *et al.* A clinical benchmark of public self-supervised pathology foundation models. *Nat. Commun.* **16**, 3640 (2025).

[22] Neidlinger, P. *et al.* Benchmarking foundation models as feature extractors for weakly supervised computational pathology. *Nat. Biomed. Eng.* **10**, 1113–1123 (2026).

[23] Adleberg, J. *et al.* Predicting patient demographics from chest radiographs with deep learning. *J. Am. Coll. Radiol.* **19**, 1151–1161 (2022).

[24] Gichoya, J. W. *et al.* AI recognition of patient race in medical imaging: a modelling study. *Lancet Digit. Health* **4**, e406–e414 (2022).

[25] Yang, Y. *et al.* Demographic bias of expert-level vision–language foundation models in medical imaging. *Sci. Adv.* **11**, eadq0305 (2025).

[26] Vaidya, A. *et al.* Demographic bias in misdiagnosis by computational pathology models. *Nat. Med.* **30**, 1174–1190 (2024).

[27] Chen, S. *et al.* Predicting patient self-reported race from skin histological images with deep learning. In *Workshop on Fairness of AI in Medical Imaging (FAIMI), MICCAI*, vol. 15976 of *Lecture Notes in Computer Science*, 104–114 (Springer, 2025).

[28] Ong Ly, C. *et al.* Shortcut learning in medical AI hinders generalization: method for estimating AI model generalization without external data. *npj Digit. Med.* **7**, 124 (2024).

[29] Jones, C. *et al.* A causal perspective on dataset bias in machine learning for medical imaging. *Nat. Mach. Intell.* **6**, 138–146 (2024).

[30] Yang, Y., Zhang, H., Gichoya, J. W., Katabi, D. & Ghassemi, M. The limits of fair medical imaging AI in real-world generalization. *Nat. Med.* **30**, 2838–2848 (2024).

[31] Lin, S.-Y. *et al.* Contrastive learning enhances fairness in pathology artificial intelligence systems. *Cell Rep. Med.* **6**, 102527 (2025).

[32] Howard, F. M. *et al.* The impact of site-specific digital histology signatures on deep learning model accuracy and bias. *Nat. Commun.* **12**, 4423 (2021).

[33] Dehkharghanian, T. *et al.* Biased data, biased AI: deep networks predict the acquisition site of TCGA images. *Diagn. Pathol.* **18**, 67 (2023).

[34] Huang, Y. *et al.* Knowledge-guided adaptation of pathology foundation models effectively improves cross-domain generalization and demographic fairness. *Nat. Commun.* **16**, 11485 (2025).

[35] Oakden-Rayner, L. *et al.* Hidden stratification causes clinically meaningful failures in machine learning for medical imaging. In *Proceedings of the ACM Conference on Health, Inference, and Learning*, 151–159 (2020).

[36] OpenAI. GPT-5 system card. Tech. Rep., OpenAI (2025). URL https://cdn.openai.com/gpt-5-system-card.pdf. 13 August 2025.

[37] Weng, Z. *et al.* GrandQC: A comprehensive solution to quality control problem in digital pathology. *Nat. Commun.* **15**, 10685 (2024).

[38] Campanella, G. *et al.* Computational pathology at health system scale – self-supervised foundation models from three billion images. *arXiv preprint arXiv:2310.07033* (2023).

[39] Ilse, M., Tomczak, J. M. & Welling, M. Attention-based deep multiple instance learning. In *Proceedings of the 35th International Conference on Machine Learning*, vol. 80 of *Proceedings of Machine Learning Research*, 2127–2136 (PMLR, 2018). URL https://proceedings.mlr.press/v80/ilse18a.html.

[40] Lu, M. Y. *et al.* Data-efficient and weakly supervised computational pathology on whole-slide images. *Nat. Biomed. Eng.* **5**, 555–570 (2021).

[41] U.S. Census Bureau. Hispanic or Latino origin by race, New York City (American Community Survey 2024 1-year estimates, table B03002) (2025). URL https://data.census.gov/table/ACSDT1Y2024.B03002?g=160XX00US3651000. Accessed 2026-07-23.

[42] Lu, M., Yang, Z., Feng, Q. *et al.* The characteristics and prognostic value of signet ring cell histology in gastric cancer: a retrospective cohort study of 2199 consecutive patients. *Medicine (Baltimore)* **95**, e4052 (2016).

[43] Choi, Y. *et al.* Sex-based differences in histology, staging, and prognosis among 2983 gastric cancer surgery patients. *World journal of gastroenterology* **28**, 933–947 (2022).

[44] Kodama, M. *et al.* Gastric mucosal changes, and sex differences therein, after helicobacter pylori eradication: A long-term prospective follow-up study. *Journal of gastroenterology and hepatology* **36**, 2210–2216 (2021).

[45] Kato, S. *et al.* Sex differences in mucosal response to helicobacter pylori infection in the stomach and variations in interleukin-8, cox-2 and trefoil factor family 1 gene expression. *Alimentary pharmacology & therapeutics* **20 Suppl 1**, 17–24 (2004).

[46] Figueroa, J. D. *et al.* Terminal duct lobular unit involution of the normal breast: implications for breast cancer etiology. *Journal of the National Cancer Institute* **106** (2014).

[47] Radisky, D. C., Visscher, D. W., Frank, R. D. *et al.* Natural history of age-related lobular involution and impact on breast cancer risk. *Breast Cancer Res. Treat.* **155**, 423–430 (2016).

[48] Sandhu, R., Chollet-Hinton, L., Kirk, E. L., Midkiff, B. & Troester, M. A. Digital histologic analysis reveals morphometric patterns of age-related involution in breast epithelium and stroma. *Human pathology* **48**, 60–8 (2016).

[49] Ogony, J. *et al.* Towards defining morphologic parameters of normal parous and nulliparous breast tissues by artificial intelligence. *Breast cancer research : BCR* **24**, 45 (2022).

[50] Thong, H. Y., Jee, S. H., Sun, C. C. & Boissy, R. E. The patterns of melanosome distribution in keratinocytes of human skin as one determining factor of skin colour. *The British journal of dermatology* **149**, 498–505 (2003).

[51] Alaluf, S. *et al.* Ethnic variation in melanin content and composition in photoexposed and photoprotected human skin. *Pigment cell research* **15**, 112–8 (2002).

[52] Tadokoro, T. *et al.* Uv-induced dna damage and melanin content in human skin differing in racial/ethnic origin. *FASEB journal : official publication of the Federation of American Societies for Experimental Biology* **17**, 1177–9 (2003).

[53] Ahmed, F., Fitzsimmons, R., Chu, E. Y., Shin, D. B. & Takeshita, J. Frequency of skin biopsies for psoriasis by race and ethnicity. *JAMA dermatology* **160**, 1003–1005 (2024).

[54] Chau, T. *et al.* Psoriasis or not? review of 51 clinically confirmed cases reveals an expanded histopathologic spectrum of psoriasis. *Journal of cutaneous pathology* **44**, 1018–1026 (2017).

[55] Janssen, C. W., Maartmann-Moe, H., Lie, R. T. & Matre, R. Age and sex distribution of intestinal type and diffuse gastric carcinoma. *APMIS : acta pathologica, microbiologica, et immunologica Scandinavica* **99**, 78–82 (1991).

[56] Derakhshan, M. H. *et al.* Oesophageal and gastric intestinal-type adenocarcinomas show the same male predominance due to a 17 year delayed development in females. *Gut* **58**, 16–23 (2009).

[57] Kensler, K. H. *et al.* Automated quantitative measures of terminal duct lobular unit involution and breast cancer risk. *Cancer epidemiology, biomarkers & prevention* **29**, 2358–2368 (2020).

[58] Girardeau, S., Mine, S., Pageon, H. & Asselineau, D. The caucasian and african skin types differ morphologically and functionally in their dermal component. *Experimental dermatology* **18**, 704–11 (2009).

Supplementary Material

Supplementary Figures

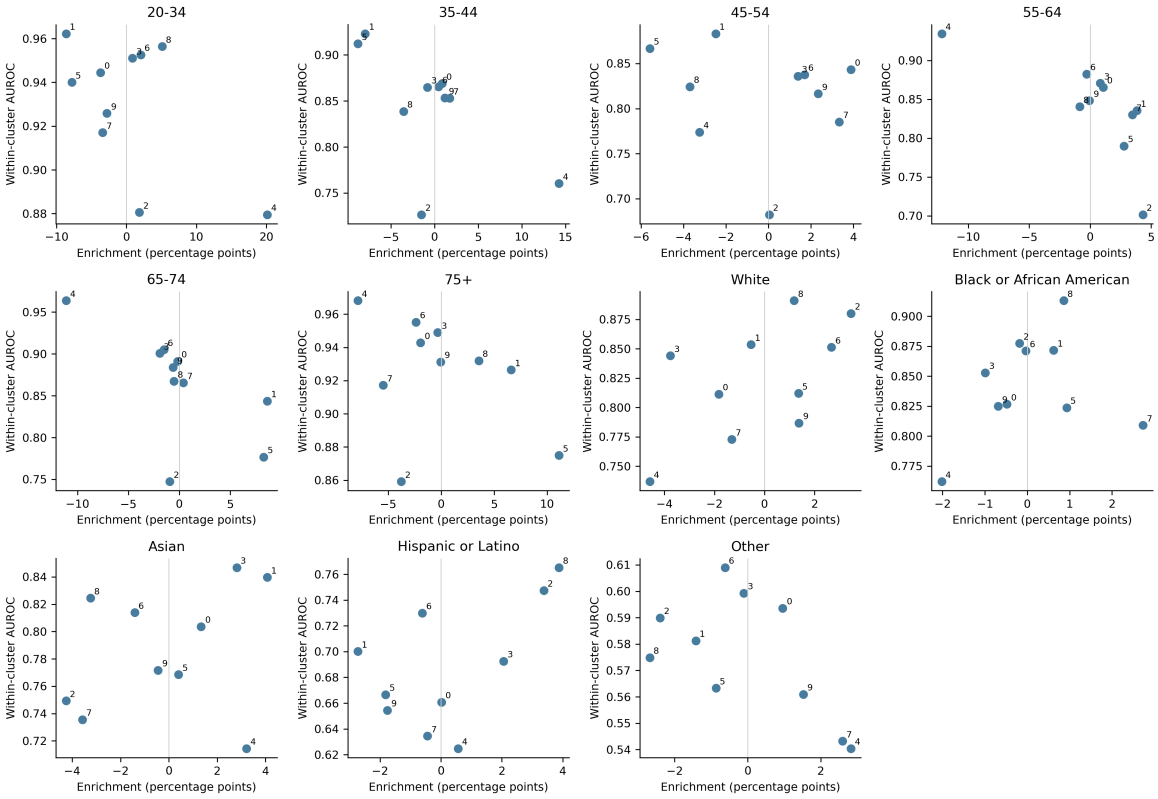


Figure S1: **Breast subgroup enrichment versus within-cluster AUROC.** Signed subgroup enrichment (percentage points relative to the eligible breast cohort) versus within-cluster subgroup AUROC under S1; each point is one canonical diagnosis cluster, labeled by cluster index. These are the per-cluster values underlying Fig. 3E.

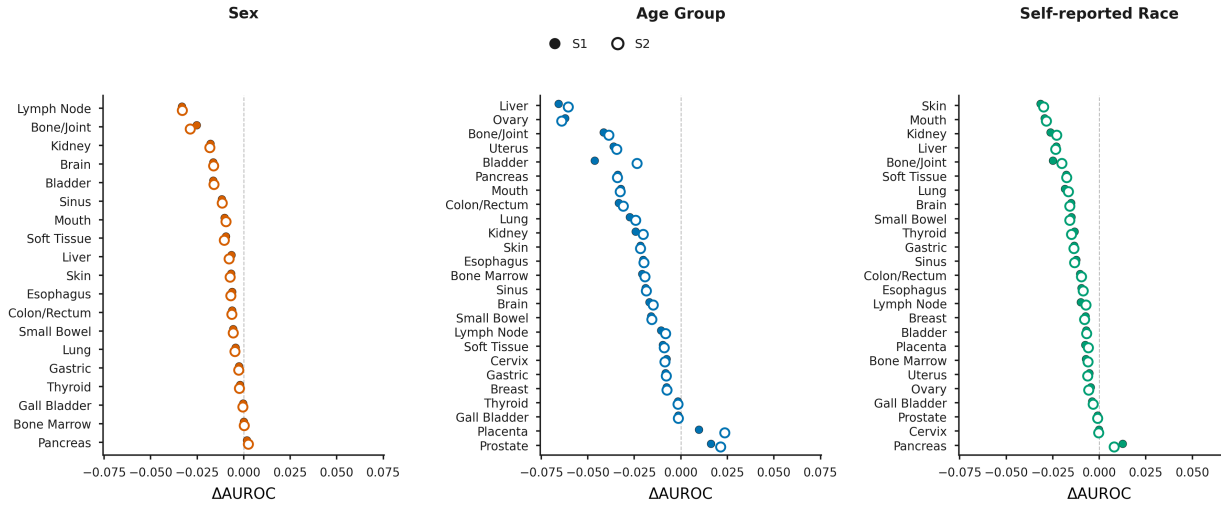


Figure S2: **Pan-organ cluster-stratified versus pooled AUROC.** Size-weighted pooled-versus-cluster-stratified AUROC under S1 across the 69 organ–demographic combinations (25 age-group, 25 self-reported-race, and 19 sex). Per-organ values appear in Supplementary Tables S7–S8.

Cohort summary

Table S1: **MSHS cohort summary.** Cohort hierarchy and demographic composition. Sex and self-reported race are patient-level; age is case-level. Sex and self-reported-race percentages use all 257,322 patients, including unknown or excluded labels, as the denominator. Age-group percentages use the 318,174 cases with known age, excluding the "Unknown/excluded" row.

Category	Subgroup	n	%
Cohort hierarchy			
	Patients	257,322	—
	Cases	327,483	—
	Specimens	731,972	—
	Whole-slide images	1,302,440	—
Sex (patient level)			
	Total with valid sex	*255,382*	
	Female	159,411	62.0
	Male	95,971	37.3
	Excluded (Indeterminate / Unknown)	1,940	0.8
Self-reported race (patient level)			
	Total with valid race	*207,500*	
	White	90,761	35.3
	Hispanic or Latino	47,220	18.4
	Black or African American	36,388	14.1
	Asian	18,457	7.2
	Other†	14,674	5.7
	Excluded (Unknown)	49,822	19.4
Age at case (continuous, case level)			
	Mean ± SD (years)	53.0 ± 17.8	
	Median [IQR]	54 [40–67]	
Age group (case level, model bins)‡			
	Total with known age	*318,174*	
	20–34	48,126	15.1
	35–44	50,160	15.8
	45–54	58,635	18.4
	55–64	64,503	20.3
	65–74	59,356	18.7
	≥75	37,394	11.8
	Unknown/excluded	9,309	—
Cases per patient			
	Mean ± SD	1.27 ± 0.72	—
	Median [IQR]	1 [1–1]	—
Specimens per case			
	Mean ± SD	2.24 ± 2.17	—
	Median [IQR]	1 [1–3]	—
Slides per case			
	Mean ± SD	4.27 ± 7.27	—
	Median [IQR]	2 [1–4]	—

† "Other" consolidates Native Hawaiian or Other Pacific Islander, American Indian or Alaska Native, and Other Race.

‡ Age groups include cases aged ≥20 years; "Unknown/excluded" includes cases with missing age or age <20 years.

Per-organ cohort scale and composition

Table S2: **Per-organ cohort scale.** Unique patient, case, specimen, and slide counts for all 25 study organs in the MSHS 2025 cohort, ordered by descending slide count. Counts are derived after specimen organ normalization and slide-readiness filtering (feature and coordinate files present).

Organ	**Patients**	**Cases**	**Specimens**	**Slides**
Breast	37,426	46,145	75,781	263,230
Colon/Rectum	54,976	60,496	144,880	175,918
Prostate	8,814	9,880	58,135	142,270
Lymph Node	14,277	15,400	28,473	84,598
Uterus	17,014	19,795	22,915	79,630
Gastric	39,205	43,135	67,104	72,363
Skin	29,581	32,938	41,887	58,824
Placenta	13,766	14,592	14,795	50,946
Small Bowel	26,228	28,643	37,098	45,191
Thyroid	3,197	3,322	4,355	42,999
Cervix	10,831	13,337	30,815	35,644
Esophagus	18,726	20,689	31,458	31,559
Bone/Joint	12,344	13,808	16,869	30,352
Soft Tissue	10,099	10,684	13,684	28,628
Kidney	4,164	4,690	9,606	21,361
Bone Marrow	6,177	11,386	29,563	20,844
Mouth	6,759	7,431	12,953	19,877
Bladder	3,192	4,342	5,844	16,794
Ovary	2,553	2,592	3,487	14,689
Sinus	4,458	4,703	11,772	13,864
Lung	2,715	3,080	4,092	11,362
Liver	3,313	3,635	4,287	11,243
Gallbladder	5,506	5,517	5,562	9,928
Brain	2,323	2,458	4,144	8,926
Pancreas	814	925	1,009	6,089
Full cohort	*257,322*	*327,483*	*731,972*	*1,302,440*

Full-cohort totals include records outside the 25-organ, slide-ready population represented by the individual rows. Patient total reflects unique individuals in the full cohort; per-organ patient counts sum to more than the cohort total because patients contributing to multiple organ types are counted once per organ.

Table S3: **Per-organ patient-level demographic composition.** Within-organ percentages of patients by sex and self-reported race. The denominator is the full per-organ patient count (Supplementary Table S2); patients with other or unknown sex or unknown self-reported race are included in the denominator but not shown, so rows do not sum to 100%, and the unknown fraction varies substantially across organs. Organs are ordered by descending slide count.

	Sex (%)		Self-reported Race (%)				
Organ	**F**	**M**	**White**	**Hisp**	**Black**	**Asian**	**Other**
Breast	94.7	1.0	25	12	11	6	4
Colon/Rectum	48.1	51.7	38	18	14	6	6
Prostate	0.0	99.9	44	17	19	5	6
Lymph Node	60.2	38.1	38	18	17	12	4
Uterus	99.4	0.4	33	22	22	9	5
Gastric	58.1	41.8	31	25	16	6	6
Skin	51.1	48.5	40	14	11	5	5
Placenta	99.9	0.1	45	20	15	9	5
Small Bowel	55.3	44.6	38	18	13	5	6
Thyroid	75.0	24.9	37	20	13	21	4
Cervix	99.8	0.1	37	17	14	10	6
Esophagus	51.7	48.2	39	18	12	5	6
Bone/Joint	52.1	47.8	38	23	19	6	5
Soft Tissue	46.1	53.7	37	24	18	8	6
Kidney	41.1	58.8	32	24	23	10	6
Bone Marrow	45.9	54.0	41	18	19	7	8
Mouth	47.6	52.1	33	13	8	8	5
Bladder	26.3	73.6	51	18	14	7	5
Ovary	99.8	0.2	40	21	19	12	5
Sinus	39.7	60.1	44	17	9	10	7
Lung	50.2	49.6	34	22	24	9	7
Liver	53.0	46.8	32	26	17	10	7
Gallbladder	68.5	31.4	27	38	12	9	8
Brain	54.2	45.7	32	22	19	11	6
Pancreas	48.2	51.8	37	25	20	10	4

F = Female; M = Male; Hisp = Hispanic or Latino; Black = Black or African American.

Diagnosis extraction

Supplementary Note S1. Specimen-level diagnoses were extracted from free-text pathology reports with a large language model (Azure OpenAI, GPT-5 mini) returning output constrained to a JSON schema. For each report the model emitted a list of specimens; each specimen carried an identifier (the specimen letter, e.g. "A"), an anatomic source, a normalized organ label drawn from the 25 study organ groups plus an *Other* category, and a diagnosis string. The instruction protocol directed the model to: (i) split each report into its constituent specimens using the explicit specimen headers; (ii) take the anatomic source and diagnosis preferentially from the *Diagnosis / Final Diagnosis* section, falling back to the specimen-source field only when the location was absent there; (iii) keep the diagnosis text *verbatim*, concatenating relevant *Addendum*, *Comment*, and *Note* sections while deduplicating repeated statements; (iv) resolve conflicts by the priority Final Diagnosis > Addendum > Comment > Note; and (v) never invent fields or facts, ignoring billing codes and boilerplate. Only the extracted specimen-level diagnosis text was used downstream; no protected health information was retained in the derived data.

Diagnostic spectrum embedding

Supplementary Note S2. The diagnostic-spectrum map in Fig. 1B was generated from the extracted specimen-level diagnosis text (Supplementary Note S1). Of 731,204 specimens with non-empty diagnosis text, 51,264 mapped to the *Other* organ category or lacked an organ label and were excluded, leaving 679,940 specimens from the 25 study organs. Diagnosis strings were embedded with Azure OpenAI `text-embedding-3-large` (3,072 dimensions). Each specimen was assigned to one of four broad categories by a rule-based mapping of the diagnosis text: neoplastic (n = 176,625; 26.0%), normal (n = 166,658; 24.5%), inflammatory, including infectious findings (n = 143,816; 21.2%), and other (n = 192,841; 28.4%), comprising non-neoplastic structural findings, tissue injury or degenerative changes, and diagnoses not matched by any rule (56.6% of the other category). To prevent high-volume organs and categories from dominating the layout, a reference set of 99,949 specimens was sampled with balanced quotas across organ × category cells (up to 1,225 per cell). Embeddings were reduced to 50 principal components (65.7% of variance explained), and a single UMAP was fitted on the reference set (cosine distance, 50 neighbours, minimum distance 0.5, fixed random seed); the remaining 579,991 specimens were projected into the fitted embedding. Because templated sign-out text yields near-identical embeddings, dense islands reflect reporting conventions rather than prevalence. The 20 labelled example diagnoses (five per category) were reviewed by pathologists, and the category of the displayed labels follows that review; the rule-based assignment used for the percentages was not modified, so a small number of individual specimens may be categorized differently from the pathologists' assessment.

Supplementary Methods

1.1 Grouped training and epoch exposure

Grouped balancing for S3 and $\mathrm{S3_{RND}}$ operated on unique pathology cases, with each case counted once in the candidate training pool. Within a grouping pool p, let n_{pg} denote the number of cases in demographic class g. The balancing target was the largest available class count, $n_p^{\max} = \max_{g\in\{1,\ldots,G\}} n_{pg}$. A class was retained only when $n_p^{\max}/n_{pg} \leq 50$; classes requiring greater oversampling were dropped, and a pool with fewer than two retained classes was excluded from group construction. Classes below $n_p^{\max}$ were oversampled by cycling through shuffled case lists to that target; the largest class was retained in full, without subsampling majority-class cases. The balanced class lists were assembled into training groups containing one case from each of the G retained demographic classes. Each case was then represented by its full case-level MIL bag.

S3 and its random grouped-training control used this formulation. $\mathrm{S3_{RND}}$ applied grouped demographic balancing once to the full, undifferentiated training pool; it did not use diagnosis clusters or randomized cluster assignments and served as the non-semantic global grouped-balancing control. S3 applied the same formulation separately within the diagnosis-context clusters defined above. Clusters with fewer than two retained demographic classes were excluded, and groups from the retained clusters were combined for training. $\mathrm{S3_{RND}}$ is reported as a supporting control to S3.

S1 and S2 processed cases individually and computed loss case by case. Each S3 or $\mathrm{S3_{RND}}$ training example was a demographic group; the case-level cross-entropy losses were summed across group members before gradient accumulation and the optimizer step. Thus, although all regimes retained the same case-level MIL prediction unit, grouped training changed the effective batch structure and case presentations per epoch relative to S2. Grouped training used a gradient-accumulation setting of 8.

The S1 per-epoch case target was $N_{\mathrm{epoch}} = \min\{N_{\mathrm{train}}, \max[\mathrm{round}(0.5N_{\mathrm{train}}), 11{,}018]\}$. S2

sampled $\max\{32, \text{round}(N_{\text{epoch}}/G)\}$ cases per target class, where G is the number of target classes. Both grouped regimes instead capped the number of groups presented per epoch using a tiered rule: all groups when at most 512 were available; 256 groups when at most 2,048 were available; 512 groups when at most 8,192 were available; and 1,024 groups for larger pools. These dataset-size-aware caps were computational design choices, not scientific controls, and contribute to the exposure difference between S2 and S3.

Training-side cluster-assignment sensitivity. Ties in case-level cluster voting were resolved by specimen row order, affecting 0.3–35.2% of training cases across organ–demographic combinations. Rebuilding groups with alternative deterministic tie-breaking rules retained at least 99.6% training-case overlap. Relabeling production groups using the lowest tied cluster index increased the mean residual class–cluster Cramér's V by 0.016, compared with 0.146 in the unbalanced pool. This group-construction check did not retrain models or establish an effect on AUROC.

1.2 Cluster-stratified evaluation

For cluster-stratified evaluation, specimen-level assignments were aggregated by majority vote; ties were resolved by the highest summed centroid similarity, with any remaining tie resolved by the lowest cluster index. The canonical breast evaluation retained 5,112 tied cases. This differs from S3 training assignment, which resolves ties by specimen row order.

As a post-hoc check on diagnostic composition, AUROC was recomputed *within* diagnosis clusters instead of over the pooled validation set. Let A_k denote the macro one-vs.-rest AUROC computed within cluster k, restricted to the classes present in that cluster; a cluster was excluded only when a single ground-truth class was present, which leaves AUROC undefined. Writing n_k for the number of validation cases in cluster k, we compare

$$\text{AUROC}_{\text{pooled}} \qquad \text{against} \qquad \text{AUROC}_{\text{strat}} = \sum_k \frac{n_k}{\sum_j n_j} A_k,$$

where $\text{AUROC}_{\text{pooled}}$ is the ordinary macro AUROC over all validation cases and $\text{AUROC}_{\text{strat}}$ averages the within-cluster values in proportion to cluster size. The pooled statistic includes rankings between cases from different clusters, whereas $\text{AUROC}_{\text{strat}}$ contains only within-cluster rankings. The primary cluster-stratified contrast was

$$\Delta = \text{AUROC}_{\text{strat}} - \text{AUROC}_{\text{pooled}},$$

tested per organ with a paired t-test across the 10 matched MCCV folds. The same calculation after random reassignment of cluster labels served as a separate evaluation-only random-label control; it is unrelated to the S3_{RND} training regime. Drop % (defined as a fraction of above-chance pooled performance) is reported per organ in Supplementary Table S8. Δ remained the primary contrast measure throughout. Case-to-cluster matching was at least 99.4% complete for every organ and fold (lowest, pancreas), and pooled and stratified AUROC were computed over the same matched cases.

1.2.1 Breast worked example: pooled versus cluster-stratified AUROC

Fig. 3D reports $\text{AUROC}_{\text{pooled}}$, $\text{AUROC}_{\text{strat}}$ and Δ exactly as defined above, taken from the same per-fold pan-organ evaluation that underlies Supplementary Tables S7–S8 (selected $K = 10$); the breast values therefore coincide with the breast row of Supplementary Table S8. In every fold, all ten breast clusters contained at least two target classes, so all matched validation cases (8,747 for age group; 5,760–5,901 for self-reported race) contributed to both statistics.

For Fig. 3B, UMAP visualizes fixed k-means assignments; it does not define the clusters. In panel E, signed enrichment is the subgroup's within-cluster proportion minus its overall breast proportion, in percentage points. Spearman correlations use the corresponding within-cluster one-vs.-rest AUROC under S1. Enrichment uses all cases with known demographic labels, whereas AUROC uses held-out cases with the same canonical assignments. Leave-one-cluster-out ranges describe sensitivity to individual clusters, not confidence intervals.

1.3 LLM-assisted literature searching and hypothesis generation

Model, inputs, and search procedure. We used OpenAI `gpt-6-astra` on 24 September 2026 (UTC) to examine prediction of self-reported race in skin, age-group prediction in breast, and sex prediction in gastric tissue. A fixed prompt was applied separately to each example, with the organ, demographic target, and observed model results supplied as inputs. For skin, the supplied results comprised residual S3 AUROC, best-context AUROC, and their difference; other strategy-level values were verified subsequently and were not generation inputs. The three candidates were selected based on residual predictability, clinical relevance, and potential for histomorphological investigation. Context-audit values were supplied as supplementary information during literature hypothesis generation; image–context gaps were not formal candidate-selection criteria. The prompt below is a reformatted, reproducible version of the search instructions.

Retrieval used web search and NCBI PubMed ESearch/EFetch, with PMC EFetch where full text was accessible. The generation stage proposed candidate tissue or contextual explanations and linked supporting claims to publications. Contradictory and null evidence was sought alongside supporting evidence. The search was targeted and exploratory, not exhaustive or systematic.

Source checking and interpretation. In a separate pass, the same model checked citation identity with PubMed ESummary and assessed each claim against the retrieved abstract or accessible publisher or PMC full text. It recorded the source identifier, material reviewed, supporting passage where available, and limits on applicability. Claims were narrowed or excluded when the inspected material did not support them. DOI and PMID records were checked against Crossref and PubMed. Claim support was assessed by the model without independent author verification.

Applicability of the evidence. Skin pigmentation studies differed in imaging modality, population, anatomical site, and exposure, limiting transfer to routine H&E in this cohort. Breast morphometry provided cross-sectional evidence on tissue composition rather than longitudinal evidence of adipose replacement[48]. Gastric findings were specific to disease subtype, subsite, and treatment. Signet-ring and diffuse categories were distinguished, as were within-cancer subtype proportions and population incidence. The review retained null findings, including no significant sex difference in atrophy scores in the eradication study[44], similar sex-specific rates of diffuse gastric carcinoma[55,56], no adjusted association between quantitative involution measures and subsequent breast cancer risk[57], and no observed difference in dermal collagen or elastic-fibre organisation between the skin types compared[58].

Reproducible search prompt.

> **Study question.** Organ: [organ]. Demographic target: [target]. Observed model results: [supplied results]. What clinical, disease-context, workflow, or histomorphologic factors could plausibly contribute to the observed demographic-associated signal in routine H&E histopathology? The observed signal does not establish its source. Generate testable hypotheses, not a conclusive explanation.

Search scope. Search clinical and contextual explanations, including disease prevalence or subtype, diagnosis distribution, anatomic subsite, procedure or sampling, severity, treatment history, clinical workflow, exposure, and healthcare context. Also search histomorphologic explanations, including H&E-visible epithelial or cellular morphology, stroma, immune composition, fibrosis, pigmentation, adipose composition, vascular features, age-related remodeling, and other tissue features. Specify whether each proposed feature is localized to a compartment, lesion, or structure; diffuse across broader tissue architecture; or mixed. Include technical or workflow explanations when directly relevant, without requiring a separate category. Do not treat self-reported race as a direct biological variable. Consider environment, exposure, healthcare access, geography, disease distribution, ancestry-correlated factors, institutional context, and workflow where supported.

Evidence requirements. Prefer peer-reviewed primary human pathology or histology studies, other direct human tissue studies, and strong pathology reviews; use epidemiologic or clinical studies for prevalence or context hypotheses. Label findings from molecular, imaging, animal, or mechanistic studies as indirect supporting context. Look for relevant contradictory and null findings. Do not generalize across organs, populations, demographic definitions, or disease settings without labeling the extrapolation as indirect. For every retained claim, identify its source, provide a DOI, PMID, or stable URL where available, identify the supporting location where available (abstract, section, page, figure, or table), and paraphrase what the source supports. Distinguish source support from the hypothesis. Do not invent citations or supporting locations. State when only the abstract is accessible and restrict claims accordingly. If no useful morphology hypothesis is supported, say so. Do not assign arbitrary evidence scores or high, medium, or low confidence labels.

Requested output. Briefly restate the supplied observed signal without adding findings. Aim for two to five useful candidate hypotheses, returning fewer or none if warranted. For each, report its type (clinical or contextual, morphology, or workflow/technical), hypothesis, spatial scope (localized, diffuse, mixed, or not applicable), features to inspect, plausible relation to the observed signal, supporting claims and sources, alternative explanations, and remaining evidence gaps. For each supporting source, provide its citation and available identifiers, evidence type and indirectness, actual access status (open full text, institutional full text, abstract only, or not reviewed), available supporting locations, and what they support. Link each claim to its source and location. List each paper once, allowing multiple claim links. Use short paraphrases rather than long quotations. Finish with unresolved questions suitable for matching, stratification, measurement, or tissue-review checks.

Style and limits. Use concise scientific language understandable to a pathology or biomedical research collaborator. Prefer a few traceable hypotheses over broad coverage. Do not claim causality, call a candidate feature a mechanism unless directly demonstrated, treat model reasoning as evidence, attempt an exhaustive systematic review, or force a hypothesis when evidence is weak.

1.4 Age-class harmonization

1.4.1 Class-set and validation comparability

For prostate and placenta age prediction, rare age groups were excluded under the S3 class-retention rule. Prostate $S3_{RND}$ and S3 originally used different class sets; their comparison was recomputed using four common age classes (45–54, 55–64, 65–74, and 75+) and 1,954 matched validation cases in each of the ten MCCV folds. Placenta used three common classes (20–34, 35–44, and 45–54) and 2,872 matched cases per fold; its S3 comparison was unchanged. All models were evaluated at epoch 50. Macro one-vs.-rest AUROC was averaged over the common classes using their original softmax probabilities, without renormalization. Other organ-level comparisons retained their original evaluation definitions.

For prostate age, harmonized AUROC was 0.714 ± 0.008 under $S3_{RND}$ and 0.700 ± 0.010 under S3 (mean ± SD across ten folds). The paired increment was 0.0140 ± 0.0053, positive in all ten folds (paired t-test $p = 1.5 \times 10^{-5}$).

Figure 4 and Supplementary Table S9 use the harmonized prostate S3 comparison. Supplementary Table S4 retains original per-regime AUROCs. S1/S2-to-S3 comparisons for prostate and placenta remain non-class-matched; no harmonized cross-stage contrasts are reported here.

Supplementary results

Table S4: **Per-organ macro one-vs.-rest AUROC across training regimes.** Mean±SD across 10 MCCV folds under S1, S2, $S3_{RND}$, and S3 (Controlled training regimes). Dashes (—) mark sex-specific organs excluded from the sex target; bold entries follow the top-performer rule of Fig. 2.

	Sex				Age Group				Self-reported Race			
Organ	S1	S2	$S3_{RND}$	S3	S1	S2	$S3_{RND}$	S3	S1	S2	$S3_{RND}$	S3
Bladder	0.762±0.026	0.761±0.029	0.731±0.017	0.724±0.014	0.656±0.012	0.614±0.018	0.595±0.013	0.583±0.019	0.566±0.012	0.548±0.018	0.547±0.012	0.541±0.011
Bone Marrow	0.773±0.022	0.767±0.019	0.607±0.014	0.607±0.013	0.687±0.008	0.666±0.012	0.621±0.008	0.611±0.008	0.645±0.014	0.628±0.014	0.592±0.008	0.585±0.008
Bone/Joint	0.759±0.017	0.746±0.014	0.650±0.008	0.615±0.008	0.709±0.006	0.700±0.007	0.660±0.006	0.615±0.007	0.637±0.011	0.606±0.014	0.577±0.009	0.546±0.010
Brain	0.604±0.021	0.603±0.023	0.534±0.022	0.514±0.024	0.601±0.014	0.599±0.015	0.590±0.020	0.574±0.020	0.540±0.013	0.536±0.014	0.542±0.016	0.523±0.015
Breast	—	—	—	—	**0.882**±0.002	**0.878**±0.002	**0.818**±0.002	**0.816**±0.002	0.750±0.007	0.726±0.006	0.646±0.005	0.642±0.005
Cervix	—	—	—	—	0.834±0.005	0.815±0.006	0.788±0.004	**0.783**±0.004	0.647±0.008	0.633±0.008	0.607±0.008	0.605±0.007
Colon/Rectum	**0.965**±0.002	**0.962**±0.002	0.727±0.004	0.728±0.003	0.784±0.004	0.775±0.007	0.701±0.002	0.670±0.002	**0.759**±0.007	**0.737**±0.008	0.655±0.002	0.645±0.004
Esophagus	**0.872**±0.008	**0.852**±0.010	0.725±0.005	0.726±0.006	0.692±0.006	0.695±0.007	0.648±0.005	0.633±0.005	0.682±0.010	0.659±0.008	0.620±0.006	0.613±0.007
Gallbladder	**0.949**±0.010	**0.951**±0.009	0.805±0.019	0.804±0.021	0.790±0.022	0.790±0.023	0.667±0.007	0.668±0.006	0.669±0.012	0.660±0.010	0.596±0.009	0.593±0.009
Gastric	**0.970**±0.003	**0.961**±0.005	**0.861**±0.004	**0.865**±0.004	0.804±0.007	0.804±0.007	0.696±0.002	0.688±0.003	**0.776**±0.009	**0.765**±0.010	**0.700**±0.004	**0.693**±0.005
Kidney	0.777±0.015	0.776±0.016	0.681±0.013	0.680±0.010	0.682±0.010	0.683±0.010	0.618±0.012	0.589±0.010	0.602±0.016	0.589±0.019	0.579±0.010	0.545±0.010
Liver	0.787±0.016	0.788±0.018	0.644±0.023	0.643±0.020	0.669±0.008	0.668±0.008	0.646±0.011	0.602±0.009	0.605±0.012	0.599±0.012	0.578±0.014	0.553±0.012
Lung	0.660±0.016	0.662±0.016	0.599±0.017	0.594±0.017	0.732±0.009	0.716±0.009	0.661±0.011	0.653±0.014	0.626±0.014	0.613±0.012	0.598±0.012	0.582±0.009
Lymph Node	**0.960**±0.007	**0.961**±0.006	**0.854**±0.006	0.827±0.007	0.789±0.011	0.786±0.009	0.669±0.006	0.659±0.006	0.715±0.009	0.685±0.012	0.630±0.006	0.624±0.006
Mouth	0.812±0.016	0.791±0.018	0.612±0.016	0.609±0.015	0.691±0.012	0.691±0.011	0.652±0.006	0.619±0.005	0.612±0.011	0.592±0.009	0.588±0.014	0.546±0.012
Ovary	—	—	—	—	**0.850**±0.007	**0.845**±0.008	**0.805**±0.010	0.771±0.016	0.588±0.013	0.577±0.022	0.555±0.018	0.550±0.015
Pancreas	0.594±0.036	0.596±0.038	0.567±0.022	0.568±0.023	0.545±0.037	0.549±0.038	0.527±0.037	0.507±0.030	0.526±0.041	0.518±0.029	0.521±0.023	0.521±0.019
Placenta	—	—	—	—	0.615±0.083	0.577±0.070	0.574±0.017	0.572±0.017	0.734±0.012	0.705±0.012	0.622±0.008	0.621±0.010
Prostate	—	—	—	—	0.765±0.063	0.751±0.083	0.714±0.008	0.650±0.022	0.740±0.015	0.707±0.012	0.627±0.009	0.622±0.007
Sinus	**0.879**±0.013	**0.880**±0.012	0.764±0.017	0.764±0.017	0.759±0.010	0.749±0.013	0.660±0.008	0.645±0.008	0.632±0.010	0.616±0.010	0.567±0.015	0.553±0.015
Skin	**0.912**±0.006	**0.899**±0.007	0.763±0.004	0.765±0.004	0.766±0.003	0.766±0.002	0.674±0.003	0.658±0.003	**0.793**±0.006	**0.767**±0.006	**0.758**±0.007	**0.728**±0.006
Small Bowel	**0.942**±0.007	**0.925**±0.009	0.785±0.003	0.791±0.004	0.749±0.006	0.749±0.006	0.662±0.003	0.647±0.004	0.726±0.008	0.709±0.011	0.665±0.005	**0.647**±0.004
Soft Tissue	0.823±0.010	0.805±0.011	0.658±0.009	0.649±0.009	0.659±0.009	0.663±0.008	0.601±0.006	0.585±0.006	0.605±0.010	0.583±0.006	0.566±0.007	0.555±0.005
Thyroid	**0.931**±0.016	**0.936**±0.016	0.761±0.019	0.762±0.020	0.770±0.012	0.774±0.011	0.701±0.008	0.702±0.009	0.714±0.014	0.700±0.017	0.635±0.015	0.625±0.019
Uterus	—	—	—	—	**0.850**±0.003	**0.842**±0.004	0.801±0.002	**0.786**±0.003	0.653±0.005	0.644±0.005	0.608±0.005	0.604±0.004
Mean	**0.828**±0.119	**0.822**±0.118	**0.702**±0.095	**0.697**±0.097	**0.733**±0.084	**0.726**±0.086	**0.670**±0.073	**0.651**±0.075	**0.662**±0.074	**0.644**±0.070	**0.607**±0.052	**0.594**±0.053

Comparability note. This table retains the original regime-specific AUROCs, including prostate S3 AUROC of 0.650. Figure 4 and Supplementary Table S9 instead use common-class, common-case evaluation for the prostate S3 comparison. S1/S2-to-S3 age contrasts for prostate and placenta remain non-class-matched (Supplementary Method 1.4.1).

Per-subgroup specimen counts and AUROC (Fig. 2C)

Supplementary Table S5 gives the S1 and S2 cross-organ subgroup estimates and S1 training-specimen counts underlying Fig. 2C.

Additional breast diagnosis-context results

Across the ten canonical breast diagnosis clusters, case counts ranged from 2,681 (5.8%; benign skin/excision patterns) to 7,745 (16.8%; benign diagnoses with calcifications). Composition used 46,145 unique cases, including 45,750 with known age and 29,343 with known self-reported race. All ten clusters contributed to each subgroup correlation. Relative to pooled AUROC, cluster-stratified age-group AUROC changed by -0.0076 ± 0.0007 under S1 and -0.0075 ± 0.0007 under S2; self-reported-race AUROC changed by -0.0075 ± 0.0012 and -0.0080 ± 0.0012, respectively (mean±SD across ten folds; paired t-test, $p < 0.001$ for each; Fig. 3D).

Table S5: **Per-subgroup specimen counts and mean AUROC by strategy.** AUROC is the macro one-vs.-rest mean across MCCV folds, averaged across all 25 organs. For each demographic subgroup, S1 training specimen counts are summed across eligible organs within each fold and averaged over the ten MCCV folds. Δ = S2 − S1 mean AUROC.

Demographic	Subgroup	S1 training specimens (all eligible organs)	S1 AUROC	S2 AUROC	Δ (S2–S1)
Age group	20–34	103,342	0.821	0.815	−0.006
	35–44	116,083	0.727	0.713	−0.014
	45–54	158,182	0.679	0.667	−0.012
	55–64	200,409	0.674	0.664	−0.010
	65–74	197,791	0.710	0.706	−0.004
	≥75	111,581	0.800	0.802	+0.002
Self-reported race	Asian	79,958	0.679	0.670	−0.009
	Black or African American	151,836	0.753	0.735	−0.018
	Hispanic or Latino	175,836	0.619	0.593	−0.026
	Other	45,402	0.538	0.524	−0.013
	White	356,882	0.720	0.698	−0.022

Across the ten canonical clusters, signed subgroup enrichment and within-cluster AUROC under S1 were negatively correlated for all six age groups, most strongly for ages 55–64 ($\rho = -0.794$) and 65–74 ($\rho = -0.685$). Correlations were positive for White ($\rho = 0.515$), Asian ($\rho = 0.321$), Hispanic or Latino ($\rho = 0.309$), and Black or African American ($\rho = 0.152$), and negative for Other ($\rho = -0.455$; all $n = 10$ clusters). Leave-one-cluster-out ranges crossed zero for ages 20–34 and 45–54 and for Black or African American. Supplementary Fig. S1 shows the per-cluster values underlying Fig. 3E.

Diagnosis-cluster quality and demographic association

Across the 25 organs, Supplementary Table S6 reports the silhouette-selected K, silhouette score, maximum inter-centroid cosine similarity, and associations between cluster membership and demographic labels (Cramér's V). The composite criterion recommended fewer clusters in some organs with closely related diagnosis-text clusters.

Table S6: **Diagnosis-cluster quality and cluster–demographic association.** Specimen-level diagnosis embeddings were clustered by k-means per organ. **Clustered specimens** counts unique specimens entering organ-specific clustering. **Sel.** and **Rec.** are the silhouette-selected and composite-recommended K, where the composite is silhouette $\times$ (1 − maximum inter-centroid cosine similarity, **Max sim.**). Cramér's V measures the association between cluster and each demographic (χ^2 test at the selected K); all associations have unadjusted $p < 0.05$ except those marked $^{\text{n.s.}}$. Sex is omitted (—) for sex-specific organs.

		K				Cluster–demographic V		
Organ	**Clustered specimens**	**Sel.**	**Rec.**	**Silhouette**	**Max sim.**	**Race**	**Age**	**Sex**
Bladder	5,844	8	8	0.154	0.946	0.077	0.135	0.152
Bone Marrow	29,563	10	10	0.177	0.966	0.105	0.121	0.028
Bone/Joint	16,869	12	8	0.205	0.898	0.133	0.206	0.238
Brain	4,144	8	8	0.244	0.903	0.119	0.143	0.144
Breast	75,781	10	10	0.144	0.934	0.053	0.152	—
Cervix	30,815	15	15	0.231	0.946	0.043	0.110	—
Colon/Rectum	144,880	100	12	0.469	0.979	0.149	0.246	0.154
Esophagus	31,458	25	15	0.391	0.965	0.111	0.169	0.187
Gallbladder	5,562	6	6	0.229	0.953	0.077	0.083	0.133
Gastric	67,104	10	15	0.255	0.970	0.155	0.138	0.080
Kidney	9,606	8	8	0.278	0.885	0.158	0.146	0.102
Liver	4,286	15	8	0.163	0.943	0.145	0.211	0.173
Lung	4,091	6	6	0.187	0.937	0.124	0.130	0.124
Lymph Node	28,473	10	8	0.198	0.939	0.097	0.120	0.500
Mouth	12,953	10	10	0.260	0.869	0.149	0.248	0.119
Ovary	3,487	6	6	0.205	0.905	0.091	0.309	—
Pancreas	1,008	6	4	0.195	0.931	$0.084^{\text{n.s.}}$	0.171	$0.074^{\text{n.s.}}$
Placenta	14,795	12	10	0.303	0.943	0.067	0.043	—
Prostate	58,135	20	12	0.432	0.969	0.087	0.072	—
Sinus	11,772	20	20	0.276	0.920	0.147	0.192	0.100
Skin	41,887	10	10	0.211	0.871	0.224	0.211	0.216
Small Bowel	37,098	100	15	0.538	0.994	0.167	0.188	0.137
Soft Tissue	13,684	12	12	0.168	0.900	0.107	0.115	0.142
Thyroid	4,355	6	6	0.204	0.926	0.143	0.070	0.135
Uterus	22,915	12	12	0.171	0.936	0.092	0.242	—

Sensitivity to cohort size and cluster number AUROC attenuation showed no significant association with clustered-specimen count (Spearman $\rho = +0.36$, $p = 0.08$ for age group, $\rho = +0.02$ for self-reported race, and $\rho = -0.07$ for sex) or with selected K ($|\rho| \leq 0.24$, all $p > 0.3$). Mean age-group attenuation was -0.022 both where selected K exceeded the composite recommendation and where the two agreed ($p = 0.84$, Mann–Whitney test). Supplementary Table S7 compares case-weighted attenuation at the selected and recommended K under S1 and S2. Supplementary Table S8 gives per-organ pooled and stratified AUROCs under S1 at the selected K.

Cluster-stratified vs. pooled evaluation, all 69 combinations

Table S7: **Aggregate cluster-stratified evaluation.** Mean signed change $\Delta = \text{AUROC}_{\text{stratified}} - \text{AUROC}_{\text{pooled}}$ under S1 and S2, averaged across eligible organs (age group and self-reported race, 25 organs; sex, 19 organs). **Size-weighted** denotes the primary case-count-weighted evaluation; **Selected** and **Recommended** denote the K used (Supplementary Table S6). The evaluation-only random-label control permutes cluster assignments for the size-weighted contrast. Definitions are given in the Supplementary Method 1.2.

		Size-weighted Δ			
Strategy	K	**Age**	**Race**	**Sex**	**Eval. random-label Δ**
S1	Selected	-0.0216	-0.0121	-0.0095	+0.0006
S1	Recommended	-0.0201	-0.0114	-0.0086	+0.0005
S2	Selected	-0.0190	-0.0118	-0.0098	+0.0009
S2	Recommended	-0.0175	-0.0113	-0.0089	+0.0008

Table S8: **Per-organ pooled versus cluster-stratified AUROC (S1, selected K). Cl.-strat.** is the size-weighted mean of within-cluster AUROC; Δ = Cl.-strat. − Pooled. **Drop %** = $\Delta/(\text{Pooled}-0.5)\times 100$ is secondary and unstable for near-chance rows (Pooled < 0.60). Significance is from paired t-tests on Δ across 10 MCCV folds ($^{*}p < 0.05$, $^{**}p < 0.01$, $^{***}p < 0.001$; $^{\text{n.s.}}$ not significant; unadjusted and exploratory because MCCV folds overlap). Dashes (—) mark sex-specific organs excluded from the sex target.

	Age			**Race**			**Sex**		
Organ	Pooled	Cl.-strat.	Drop %	Pooled	Cl.-strat.	Drop %	Pooled	Cl.-strat.	Drop %
Bladder	0.656	0.610	-29.7%***	0.566	0.559	-10.8%***	0.762	0.745	-6.2%***
Bone Marrow	0.687	0.666	-11.1%***	0.645	0.638	-5.0%***	0.773	0.773	+0.0%$^{\text{n.s.}}$
Bone/Joint	0.709	0.667	-19.9%***	0.637	0.612	-18.2%***	0.759	0.734	-9.7%***
Brain	0.601	0.584	-16.8%**	0.540	0.525	-37.6%**	0.604	0.588	-15.8%***
Breast	0.882	0.874	-2.0%***	0.750	0.743	-3.0%***	—	—	—
Cervix	0.834	0.827	-2.3%***	0.647	0.647	-0.1%$^{\text{n.s.}}$	—	—	—
Colon/Rectum	0.784	0.751	-11.7%***	0.759	0.749	-4.0%***	0.965	0.959	-1.3%***
Esophagus	0.692	0.672	-10.6%***	0.682	0.672	-5.3%***	0.872	0.866	-1.7%***
Gallbladder	0.790	0.788	-0.5%**	0.669	0.665	-2.3%***	0.949	0.948	-0.1%$^{\text{n.s.}}$
Gastric	0.804	0.796	-2.7%***	0.776	0.763	-4.9%***	0.970	0.968	-0.5%***
Kidney	0.682	0.657	-13.4%***	0.602	0.576	-25.8%***	0.777	0.759	-6.4%***
Liver	0.669	0.604	-38.7%***	0.605	0.582	-22.1%***	0.787	0.780	-2.3%**
Lung	0.732	0.705	-11.8%***	0.626	0.607	-14.8%***	0.660	0.655	-2.7%*
Lymph Node	0.789	0.779	-3.7%***	0.715	0.705	-4.6%***	0.960	0.927	-7.2%***
Mouth	0.691	0.659	-16.9%***	0.612	0.583	-26.1%***	0.812	0.802	-3.3%***
Ovary	0.850	0.788	-17.7%***	0.588	0.583	-5.2%**	—	—	—
Pancreas	0.545	0.511	-75.5%*	0.526	0.539	+47.4%*	0.594	0.596	+1.8%$^{\text{n.s.}}$
Placenta	0.615	0.625	+8.4%$^{\text{n.s.}}$	0.734	0.726	-3.2%***	—	—	—
Prostate	0.765	0.781	+6.1%$^{\text{n.s.}}$	0.740	0.740	-0.4%$^{\text{n.s.}}$	—	—	—
Sinus	0.759	0.740	-7.3%***	0.632	0.619	-9.4%***	0.879	0.867	-3.1%***
Skin	0.766	0.744	-8.2%***	0.793	0.762	-10.8%***	0.912	0.905	-1.7%***
Small Bowel	0.749	0.733	-6.5%***	0.726	0.711	-6.6%***	0.942	0.936	-1.3%***
Soft Tissue	0.659	0.649	-6.1%***	0.605	0.588	-16.9%***	0.823	0.814	-2.9%***
Thyroid	0.770	0.769	-0.6%$^{\text{n.s.}}$	0.714	0.701	-6.2%**	0.931	0.929	-0.5%*
Uterus	0.850	0.814	-10.3%***	0.653	0.648	-3.6%***	—	—	—

Per-organ AUROC differences between grouped-training regimes

Table S9: **Per-organ AUROC differences between $S3_{RND}$ and S3.** Difference = AUROC($S3_{RND}$)−AUROC(S3), mean across 10 matched MCCV folds; positive values indicate lower AUROC under diagnosis-context stratification. Significance is from paired t-tests on fold-level differences ($^{*}p < 0.05$, $^{**}p < 0.01$, $^{***}p < 0.001$; $^{\text{n.s.}}$ not significant); p-values are unadjusted; BH-adjusted values for this comparison appear in Supplementary Table S10 (52 of 69 combinations, 75%, have unadjusted $p < 0.05$: 22/25 age, 22/25 self-reported race, and 8/19 sex; all 52 also have within-target BH $q < 0.05$). Fold dependence remains uncorrected, so these tests are exploratory. Dashes (—) mark sex-specific organs excluded from the sex target. Prostate age uses common-class, common-case evaluation; all other differences retain their original definitions (Supplementary Method 1.4.1).

Organ	Age Group	Self-reported Race	Sex
Bladder	+0.0116*	+0.0066**	+0.0070**
Bone Marrow	+0.0099***	+0.0070**	−0.0000$^{\text{n.s.}}$
Bone/Joint	+0.0455***	+0.0310***	+0.0350***
Brain	+0.0165***	+0.0184***	+0.0199***
Breast	+0.0016***	+0.0041***	—
Cervix	+0.0050***	+0.0011$^{\text{n.s.}}$	—
Colon/Rectum	+0.0311***	+0.0095***	−0.0004$^{\text{n.s.}}$
Esophagus	+0.0151***	+0.0072***	−0.0011$^{\text{n.s.}}$
Gallbladder	−0.0012$^{\text{n.s.}}$	+0.0033**	+0.0003$^{\text{n.s.}}$
Gastric	+0.0076***	+0.0068***	−0.0034**
Kidney	+0.0296***	+0.0340***	+0.0010$^{\text{n.s.}}$
Liver	+0.0440***	+0.0255***	+0.0012$^{\text{n.s.}}$
Lung	+0.0079**	+0.0157***	+0.0050**
Lymph Node	+0.0104***	+0.0065***	+0.0273***
Mouth	+0.0332***	+0.0414***	+0.0026$^{\text{n.s.}}$
Ovary	+0.0340***	+0.0050*	—
Pancreas	+0.0199**	+0.0007$^{\text{n.s.}}$	−0.0008$^{\text{n.s.}}$
Placenta	+0.0017$^{\text{n.s.}}$	+0.0008$^{\text{n.s.}}$	—
Prostate	+0.0140***	+0.0050**	—
Sinus	+0.0153***	+0.0142***	+0.0005$^{\text{n.s.}}$
Skin	+0.0155***	+0.0298***	−0.0012$^{\text{n.s.}}$
Small Bowel	+0.0153***	+0.0182***	−0.0061***
Soft Tissue	+0.0161***	+0.0108***	+0.0096***
Thyroid	−0.0008$^{\text{n.s.}}$	+0.0101**	−0.0013$^{\text{n.s.}}$
Uterus	+0.0151***	+0.0042***	—

Exploratory paired comparisons across training regimes

MCCV validation sets overlapped across folds (mean pairwise Jaccard index, 0.111), so fold-level differences were not independent. BH adjustment addresses multiplicity but not fold dependence; the paired tests are exploratory comparisons rather than confirmatory evidence.

Table S10: **Exploratory paired training-regime comparisons.** Mean AUROC differences across ten matched MCCV folds, the number of folds with a positive difference (n_+), nominal paired-t p-values, and within-target BH q-values. $\Delta_2 = \text{S2} - \text{S1}$ uses the native Figure 2 convention; $\Delta_3 = \text{AUROC}(\text{S3}_{\text{RND}}) - \text{AUROC}(\text{S3})$ uses the finalized Figure 4 comparison, including common-class, common-case prostate and placenta age evaluation. Positive Δ_3 indicates lower AUROC under cluster-constrained training, matching Figure 4 and Supplementary Table S9; n_+ counts strictly positive fold differences (exact zeros are excluded).

	S2 relative to S1				S3_{RND} minus S3			
Organ	Δ_2	n_+	p	q	Δ_3	n_+	p	q
Sex								
Bladder	-0.0004	5	0.840	0.840	+0.0070	9	0.008	0.019
Bone Marrow	-0.0068	1	0.003	0.006	-0.0000	6	0.998	0.998
Bone/Joint	-0.0128	0	2.1e-05	5.7e-05	+0.0350	10	1.1e-06	1.1e-05
Brain	-0.0013	4	0.404	0.481	+0.0199	10	1.5e-04	5.5e-04
Colon/Rectum	-0.0024	0	2.3e-06	8.7e-06	-0.0004	5	0.674	0.822
Esophagus	-0.0206	0	7.0e-10	1.3e-08	-0.0011	3	0.460	0.794
Gallbladder	+0.0022	8	0.044	0.069	+0.0003	6	0.779	0.822
Gastric	-0.0097	0	2.6e-05	6.2e-05	-0.0034	1	0.001	0.004
Kidney	-0.0009	5	0.499	0.558	+0.0010	6	0.595	0.822
Liver	+0.0014	8	0.399	0.481	+0.0012	6	0.692	0.822
Lung	+0.0024	8	0.039	0.067	+0.0050	9	0.006	0.018
Lymph Node	+0.0004	5	0.282	0.412	+0.0273	10	3.9e-08	7.5e-07
Mouth	-0.0207	0	1.2e-05	3.8e-05	+0.0026	6	0.324	0.615
Pancreas	+0.0011	4	0.568	0.600	-0.0008	4	0.736	0.822
Sinus	+0.0010	5	0.405	0.481	+0.0005	5	0.776	0.822
Skin	-0.0127	0	2.7e-07	2.6e-06	-0.0012	4	0.298	0.615
Small Bowel	-0.0166	0	5.2e-07	3.3e-06	-0.0061	0	1.3e-04	5.5e-04
Soft Tissue	-0.0180	0	1.6e-06	7.6e-06	+0.0096	10	1.2e-04	5.5e-04
Thyroid	+0.0049	9	0.024	0.047	-0.0013	4	0.643	0.822
Age group								
Bladder	-0.0422	0	1.1e-05	4.7e-05	+0.0116	9	0.027	0.030
Bone Marrow	-0.0215	0	5.3e-06	3.3e-05	+0.0099	10	2.1e-06	4.1e-06
Bone/Joint	-0.0092	0	9.1e-06	4.6e-05	+0.0455	10	1.2e-08	5.1e-08
Brain	-0.0015	3	0.164	0.241	+0.0165	10	1.5e-05	2.4e-05
Breast	-0.0036	0	1.4e-06	1.6e-05	+0.0016	10	2.5e-04	3.3e-04
Cervix	-0.0190	0	6.7e-07	1.6e-05	+0.0050	10	2.2e-05	3.3e-05
Colon/Rectum	-0.0086	0	6.5e-05	2.0e-04	+0.0311	10	4.8e-13	1.2e-11
Esophagus	+0.0028	10	2.9e-05	1.0e-04	+0.0151	10	1.2e-08	5.1e-08
Gallbladder	+0.0001	5	0.850	0.859	-0.0012	3	0.144	0.157
Gastric	-0.0000	6	0.859	0.859	+0.0076	10	2.9e-08	9.0e-08
Kidney	+0.0010	5	0.384	0.505	+0.0296	10	1.2e-06	2.4e-06
Liver	-0.0019	3	0.043	0.082	+0.0440	10	2.5e-07	5.8e-07
Lung	-0.0160	1	8.2e-04	0.002	+0.0079	8	0.004	0.005
Lymph Node	-0.0031	2	0.149	0.232	+0.0104	10	9.8e-08	2.7e-07
Mouth	-0.0004	4	0.378	0.505	+0.0332	10	2.7e-08	9.0e-08
Ovary	-0.0056	1	0.004	0.008	+0.0340	10	2.8e-06	5.0e-06
Pancreas	+0.0039	6	0.693	0.788	+0.0199	8	0.004	0.004
Placenta	-0.0385	3	0.063	0.112	+0.0017	6	0.229	0.238
Prostate	-0.0145	5	0.501	0.626	+0.0140	10	1.5e-05	2.4e-05
Sinus	-0.0097	0	0.002	0.004	+0.0153	10	4.0e-05	5.6e-05
Skin	+0.0000	4	0.834	0.859	+0.0155	10	2.9e-10	3.6e-09
Small Bowel	+0.0003	5	0.660	0.786	+0.0153	10	1.7e-07	4.2e-07
Soft Tissue	+0.0048	10	0.001	0.003	+0.0161	10	6.0e-09	3.7e-08
Thyroid	+0.0035	8	0.113	0.188	-0.0008	3	0.278	0.278

Supplementary Table S10 continued

Organ	Δ_2	n_+	p	q	Δ_3	n_+	p	q
Uterus	-0.0084	0	1.9e-06	1.6e-05	+0.0151	10	5.7e-09	3.7e-08
Self-reported race								
Bladder	-0.0181	0	2.7e-04	3.9e-04	+0.0066	9	0.001	0.002
Bone Marrow	-0.0171	0	9.4e-06	2.6e-05	+0.0070	9	0.007	0.009
Bone/Joint	-0.0309	0	1.7e-06	1.1e-05	+0.0310	10	1.4e-07	8.6e-07
Brain	-0.0040	3	0.129	0.134	+0.0184	10	1.9e-06	5.9e-06
Breast	-0.0236	0	1.1e-06	9.2e-06	+0.0041	10	2.5e-06	6.9e-06
Cervix	-0.0149	0	2.4e-05	5.6e-05	+0.0011	7	0.121	0.131
Colon/Rectum	-0.0224	0	9.3e-06	2.6e-05	+0.0095	10	1.1e-06	3.8e-06
Esophagus	-0.0228	0	6.8e-06	2.4e-05	+0.0072	10	1.1e-05	2.8e-05
Gallbladder	-0.0090	1	0.004	0.005	+0.0033	9	0.005	0.006
Gastric	-0.0114	0	2.6e-05	5.6e-05	+0.0068	10	1.4e-05	3.2e-05
Kidney	-0.0128	1	4.5e-04	6.2e-04	+0.0340	10	3.9e-08	3.2e-07
Liver	-0.0054	1	0.004	0.005	+0.0255	10	7.7e-07	3.2e-06
Lung	-0.0131	1	6.7e-04	8.8e-04	+0.0157	10	3.8e-05	7.3e-05
Lymph Node	-0.0292	0	3.7e-06	1.9e-05	+0.0065	10	8.5e-05	1.4e-04
Mouth	-0.0208	0	3.3e-05	6.4e-05	+0.0414	10	2.4e-07	1.2e-06
Ovary	-0.0108	2	0.018	0.019	+0.0050	8	0.034	0.038
Pancreas	-0.0083	4	0.300	0.300	+0.0007	5	0.879	0.879
Placenta	-0.0293	0	1.1e-09	2.8e-08	+0.0008	5	0.431	0.449
Prostate	-0.0339	0	7.2e-05	1.2e-04	+0.0050	8	0.006	0.007
Sinus	-0.0159	1	2.4e-04	3.7e-04	+0.0142	10	2.7e-05	5.7e-05
Skin	-0.0260	0	7.9e-09	9.9e-08	+0.0298	10	4.0e-10	9.3e-09
Small Bowel	-0.0176	0	2.7e-05	5.6e-05	+0.0182	10	7.5e-10	9.3e-09
Soft Tissue	-0.0221	0	4.1e-05	7.3e-05	+0.0108	10	4.9e-05	8.7e-05
Thyroid	-0.0141	1	0.004	0.005	+0.0101	9	0.001	0.002
Uterus	-0.0096	0	4.7e-06	2.0e-05	+0.0042	10	3.5e-04	5.5e-04